nature communications

Article

https://doi.org/10.1038/s41467-025-65900-y

The Vap33 signaling axis precisely coordinates the timing of motoneuron dendritogenesis in neural map development

Received: 20 December 2024

Accepted: 23 October 2025

Daichi Kamiyama[1,2], Rie Kamiyama[1,5], Yuri Nishida[1,5], Anthony Sego[1,2], George Berner Vining[1], Kathy Clara Bui[1,2], Miyuki Fitch[1], Hy Gia Truong Do[1], Oshri Avraham[1,2] & Takahiro Chihara[3,4]

In *Drosophila* motoneurons, spatiotemporal dendritic patterns are established in the ventral nerve cord. While many guidance cues have been identified, the mechanisms of temporal regulation remain unknown. Previously, we identified the actin modulator Cdc42 GTPase as a key factor in this process. In this report, we further identify the upstream factors that activate Cdc42. Using single-cell genetics, FRET-based imaging, and biochemical techniques, we demonstrate that the guanine nucleotide exchange factor Vav is anchored to the plasma membrane via the Eph receptor tyrosine kinase, enabling Cdc42 activation. VAMP-associated protein 33 (Vap33), a potential Eph ligand supplied non-cell-autonomously, may induce Eph autophosphorylation, initiating downstream signaling. Traditionally known as an ER-resident protein, Vap33 is secreted extracellularly at the onset of Cdc42 activation, acting as a temporal cue. In humans, VAPB—the ortholog of Vap33—is similarly secreted in the spinal cord, and its dysregulation leads to amyotrophic lateral sclerosis type 8 (ALS8). Our findings may help inform future studies on how VAPB signaling contributes to motor circuit formation in both physiological and disease contexts.

Precise synaptic connections are critical for proper ᴍ brain function during development. The brain's functionality hinges on unique patterns of connections between neuron populations, which form distinct neural maps[1–4]. The creation of these maps depends on the correct patterning of axons and dendrites, with axons targeting specific zones or laminae to connect with the dendrites of postsynaptic neurons. This process is observed in multiple brain regions, including the cerebral cortex, retina and superior colliculus, thalamus, and hippocampus[5–11]. Our understanding of the cellular principles that shape neural maps has greatly advanced through studies of sensorimotor systems[10–15]. Recent connectomic research in model organisms, such as *Drosophila melanogaster*, has further revealed individual neurons involved in assembling these intricate systems[16–28]. Additionally, a wide range of genetic tools in *Drosophila* has greatly facilitated the discovery of genes essential for organizing and developing neuronal connections. One of the most advanced areas in this research is the study of the adult olfactory map in *Drosophila*. The assembly of this neural map begins with the dendritic outgrowth and guidance of olfactory projection neurons (PNs), which lay the groundwork for a prototypical map[29–33]: Before the presynaptic olfactory receptor neuron (ORN) axons innervate the region, PNs establish their dendrites in specific territories, predefining the framework for future connections. This process has sparked significant interest in understanding how positional cues guide PN dendrites. As a result, numerous cell-surface proteins, including key guidance molecules, have been identified as critical in directing the formation of dendritic arbors and synaptic

---

[1]Department of Cellular Biology, University of Georgia, Athens, GA, USA. [2]Neuroscience Program, University of Georgia, Athens, GA, USA. [3]Program of Biomedical Science, Graduate School of Integrated Sciences for Life, Hiroshima University, Hiroshima, Japan. [4]Program of Basic Biology, Graduate School of Integrated Sciences for Life, Hiroshima University, Hiroshima, Japan. [5]These authors contributed equally: Rie Kamiyama, Yuri Nishida.

e-mail: daichi.kamiyama@uga.edu

connections[34–37]. Although the mechanisms by which dendritic arbors navigate toward their final target fields are well understood, the initial processes governing how dendrites extend into these target areas remain largely unknown.

Hints of initial dendritic outgrowth have emerged from studies on motoneurons (MNs) in the embryonic ventral nerve cord (VNC), where approximately 36 MNs reside in each hemi-segment[38–43]. These MNs extend their dendrites into specific regions of the neuropil, creating a myotopic map, a prototypical neural map[44–55]. Remarkably, the outgrowth and guidance of dendritic arbors in this system occur independently of presynaptic partners, muscles, and glia[44]. This process is largely regulated by a set of guidance molecules, including the Slit-Robo and Netrin-Frazzled signaling pathways[45–47]. In mutants lacking functional Robo or Fra receptors, dendritic arbors are misdirected. However, a closer examination reveals that while higher-order branches are significantly affected, the primary (1°) and secondary (2°) branches remain largely intact, resembling wild-type branches. This observation suggests the existence of an additional program specifically promoting the outgrowth of these initial 1° and 2° branches. As the saying goes, "A journey of a thousand miles begins with a single step," and understanding this initial step is key to unraveling the formation of this neural map and the locomotion circuit it governs.

During embryonic development, dendrites extend from the axon shaft, initiating with filopodia-like structures that emerge from the proximal region of the shaft. These filopodia eventually stabilize and form the 1° and 2° branches. Interestingly, in most motoneurons, regardless of their lineage or birth time, these filopodia appear synchronously around 13 hours after egg laying (AEL)[50–53,55–57]. This simultaneous extension, rather than a sequential outgrowth, seems to be a key feature of motoneuron development and has also been observed in the leg motoneurons during the pupal-adult transition[58]. To investigate the molecular mechanisms underlying filopodia extension, we focused on the most well-characterized motoneuron, the anterior corner cell (aCC) motoneuron. Our previous work has explored the role of Cdc42, a small Rho GTPase, which is known to be a central regulator of filopodia formation[51]. Cdc42 alternates between two conformations: an "on" state when bound to GTP and an "off" state when bound to GDP. Guanine nucleotide exchange factors (GEFs) and GTPase-activating proteins (GAPs) regulate Cdc42 by driving it into these active or inactive states, respectively[59,60]. Numerous imaging studies using Cdc42 biosensors have demonstrated that Cdc42 is activated at the base of filopodia in various cell types during their formation[61–63]. Similarly, in the aCC motoneuron, we observed Cdc42 activation at the precise locations where dendritic filopodia emerge[51]. Notably, this activation begins exactly at 13:00 AEL, coinciding with the onset of dendritic filopodia formation. This temporal synchronization suggests that Cdc42 plays a critical role as a timing cue for filopodia emergence. Supporting this hypothesis, *Cdc42* loss-of-function mutants showed a significant reduction in dendritic filopodia in aCC motoneurons, further emphasizing its importance in the process.

A similar loss-of-dendrite phenotype in *Cdc42* mutants was observed in other motoneurons[51], suggesting that the regulation of Cdc42 activation is broadly conserved across motoneurons. However, the precise molecular mechanisms controlling Cdc42 activation remain unclear. In this study, we performed a genetic screen using RNA interference (RNAi) to knock down the function of Cdc42 GEFs. Through this screening, we identified Vav, a member of the Dbl family of GEFs, as a key activator of Cdc42. Further genetic and biochemical assays revealed that the Eph receptor tyrosine kinase localizes Vav to the plasma membrane, thereby facilitating Cdc42 activation. Additionally, we discovered that VAMP-associated protein 33 (Vap33) likely functions as a ligand for the Eph receptor in this pathway. Vap33 is a type IV transmembrane protein typically localized to the endoplasmic reticulum (ER)[64,65]. However, our imaging analyses indicate that during the time of Cdc42 activation, Vap33 becomes exposed extracellularly in the VNC. This extracellular exposure may enable the Eph-Vav-Cdc42 signaling cascade to initiate filopodia formation in motoneurons in a timely manner. Importantly, dysfunction of VAPB, the human ortholog of Vap33, has been implicated in the development of a specific familial amyotrophic lateral sclerosis (ALS8)[66–68]. Our findings further suggest a potential role for VAPB signaling in establishing motor circuitry, with disruptions in this pathway possibly contributing to this familial type of ALS and beyond.

Results

The Rho Family GEF Vav Has a Cell-Autonomous Function in aCC Dendritogenesis

aCC motoneurons are located in an abdominal segment of the VNC (Fig. 1a). Our primary focus has been the investigation of the initial step of dendritic outgrowth, and we previously conducted a detailed characterization of their dendritic morphology[51,52]. To visualize these processes with high resolution, we employed a retrograde labeling approach[69]. In this method, a lipophilic dye was injected into the axon tips of fixed samples at different developmental time points. This technique enables high-density membrane labeling, allowing for the clear resolution of each dendritic branch. The initial dendritic outgrowth follows a stereotyped developmental sequence (Supplementary Fig. 1). Observations made before 11:00 AEL revealed a minimal presence of filopodia along the axons. By 13:00 AEL, filopodia began to emerge in the proximal region of the axons. Previous live imaging has shown that these filopodia exhibit dynamic behavior around 13:00 AEL, frequently extending and retracting. By 15:00 AEL, these structures become more stable, allowing for reliable quantification. By 17:00 AEL, the transition from filopodia to dendritic branches is complete, with these filopodia-like structures having matured into dendritic branches forming tertiary or higher-order branches and establishing functional synaptic connections[49,50]. We refer to these filopodia-like structures as "dendritic filopodia" and identify the period from 13:00 to 15:00 AEL as the onset of "dendritogenesis." Our previous research showed that *Cdc42* mutations resulted in a significant reduction in the number of dendritic filopodia at 15:00 AEL (9.8 ± 0.4 in wild type, 4.9 ± 0.3 in *Cdc42* $^{-/-}$, $p < 0.0001$; Student's *t*-test)[51], highlighting the critical role of Cdc42 in the dendritogenesis process of aCC motoneurons.

The role of *Cdc42* in regulating cytoskeletal dynamics for morphogenesis depends on its activation, which allows it to bind to downstream effectors[59,60]. To investigate the mechanisms underlying Cdc42 activation, we began by screening RNAi constructs targeting 18 genes that encode Cdc42 GEFs. We expressed *UAS-RNAi* constructs in aCC motoneurons using an *even-skipped-GAL4* (*eve-GAL4*) driver line[70]. The expression of the *GAL4* transgene was initiated four hours prior to the onset of dendritogenesis and continued throughout embryogenesis. This RNAi approach has proven to be exceptionally powerful, as we have previously identified numerous genes crucial for aCC morphogenesis[51,52]. Among the 18 genes screened, knocking down any one of the genes encoding Vav and RhoGEF2 resulted in a severe reduction in the number of dendritic filopodia (Supplementary Fig. 2a). To further narrow down the gene involved in dendritogenesis, we analyzed embryos homozygous for amorphic alleles of *Vav* or *RhoGEF2* (*Vav* $^{-/-}$ or *RhoGEF2* $^{-/-}$). Among these, *Vav* $^{-/-}$ embryos exhibited the most pronounced reduction in the number of dendritic filopodia (Fig. 1b and Supplementary Fig. 2b). This led us to focus on *Vav*, which encodes a cytosolic protein from the Dbl GEF superfamily. Unlike vertebrates, which possess three *VAV* genes, *Drosophila* has only one *Vav* gene[71,72]. Previous studies have shown that *Vav* is expressed early during embryogenesis and plays a critical role in axonal growth within a subset of interneurons[71]. However, in contrast to these interneurons, aCC motoneuron axon development occurs normally in *Vav* $^{-/-}$

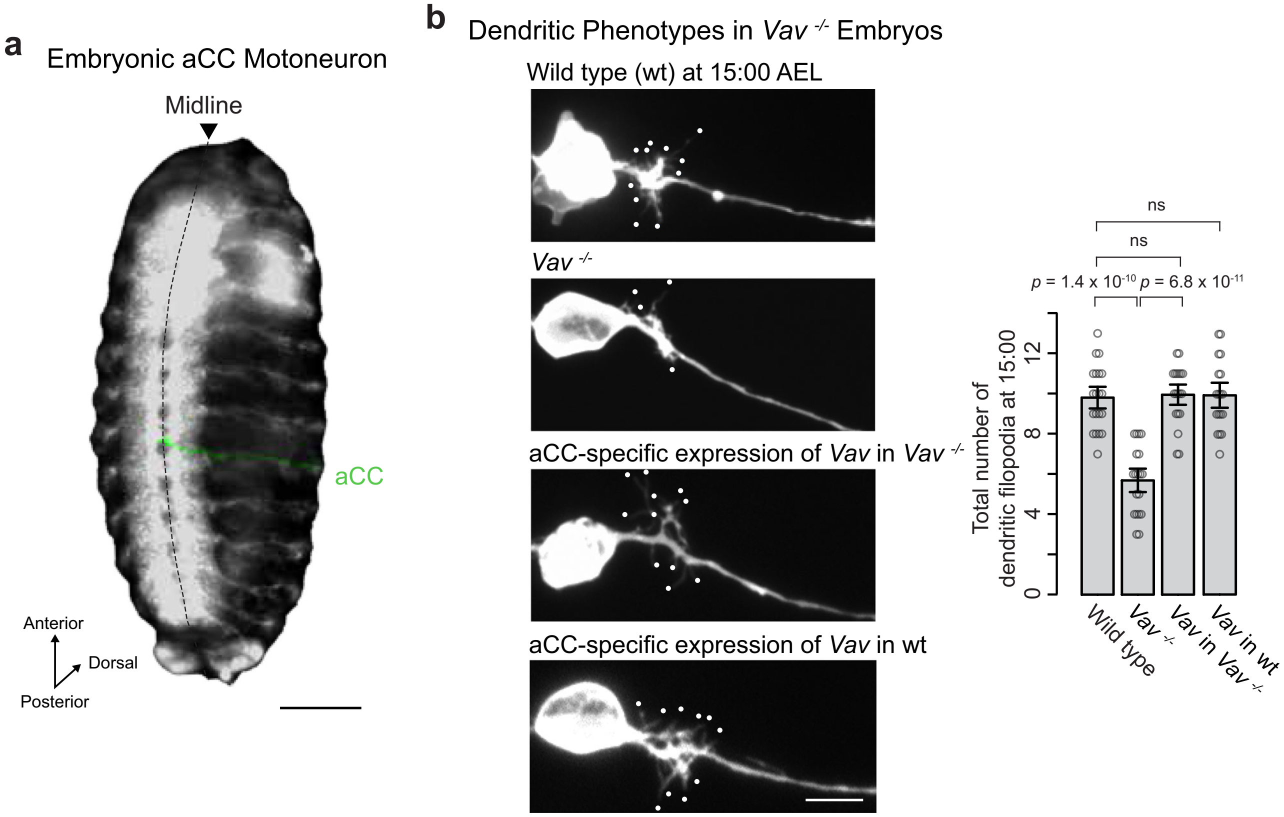

Fig. 1 | The Vav gene is essential for dendritic filopodia outgrowth. a A representative image of the aCC motoneuron (green) in abdominal segment 4 (A4) of an embryo at 15:00 after egg laying (AEL), shown in a ventral view with anterior oriented upwards. **b** Left: Representative images of dendritic outgrowth at 15:00 AEL in wild-type embryos, *Vav* knockout ($Vav^{-/-}$), and $Vav^{-/-}$ or wild-type embryos with aCC-specific Vav expression. Images are oriented with anterior upwards and dorsal to the right. Dots mark the tips of dendritic filopodia longer than 1 µm. Right: Quantification of dendritic filopodia number for each genotype. Statistical significance was determined by one-way ANOVA ($F_{3,72} = 31$, $p = 4.2 \times 10^{-13}$, followed by Tukey's multiple comparison test. "ns" indicates $p > 0.05$, indicating no significant difference. A total of 20, 19, 19, and 18 neurons were analyzed for wild type (wt), $Vav^{-/-}$, *Vav* in $Vav^{-/-}$, and *Vav* in wt, respectively. Analyses of dendritic filopodia in all other figures were also performed at 15:00 AEL. Error bars represent the mean ± SEM. Scale bars: 100 µm in (a); 5 µm in (b). Source data are provided as a Source Data file.

mutants, while dendritogenesis is severely impaired. Notably, the loss of dendritic filopodia in $Vav^{-/-}$ mutants was rescued by reintroducing *Vav* into aCC motoneurons (Fig. 1b). In parallel, aCC-specific overexpression of *Vav* in a wild-type background did not affect dendritogenesis, suggesting that proper regulation of Vav activity—rather than simply its abundance—is required for function (Fig. 1b). Together, these results demonstrate that *Vav* is a key GEF that functions in a cell-autonomous manner within aCC motoneurons to promote dendritic filopodia formation.

Cdc42 GTPase is activated by Vav in the aCC Motoneuron

To investigate whether the observed reduction in dendritic filopodia in $Vav^{-/-}$ mutants is a result of decreased Cdc42 activation, we imaged Cdc42 activity in aCC motoneurons. For this purpose, we previously generated transgenic flies expressing a fluorescence resonance energy transfer (FRET)-based Cdc42 activation probe, referred to as aProbe (Supplementary Fig. 3a)[51]. When driven by the *eve-GAL4* driver, this probe revealed the presence of a FRET signal in the cell bodies throughout development, consistent with the understanding that *Cdc42* has multiple roles in maintaining cellular homeostasis[73–75]. In addition, we detected a FRET signal in the proximal region of the axon[51]. To further quantify changes in the FRET signal over time, we measured the region where the axon shaft spans from 5 to 30 µm from the midline (Supplementary Fig. 3b). Our analysis of the FRET signals revealed the dynamic nature of Cdc42 activation (Supplementary Fig. 4): the activation is absent before 13:00 AEL but begins to be consistently observed between 13:00 and 15:00 AEL. This timing aligns with the emergence of filopodia. Furthermore, to assess the role of *Vav* in Cdc42 activation in the proximal axon region, we compared FRET signals in control flies to those in $Vav^{-/-}$ mutants at the critical time point of 15:00 AEL. We observed a significant reduction in Cdc42 activation within this region in $Vav^{-/-}$ mutants (Fig. 2a). Notably, Cdc42 activation remains normal in the cell body, suggesting that GEFs other than Vav regulate Cdc42 in this area. These findings provide strong evidence that Vav specifically regulates Cdc42 activation at the site of dendritogenesis.

The Eph receptor activates Cdc42 and plays a cell-autonomous role in Dendritogenesis

Given the consistent and temporally precise regulation of Cdc42 activation across embryos, we hypothesized that this regulation might depend on extracellular signaling molecules engaging cell surface receptors that act upstream of Vav signaling. In a previous RNAi screen of 20 cell surface receptors, we focused on their roles in dendritic filopodia formation in aCC motoneurons. Using the *eve-GAL4* driver to express *UAS-RNAi* constructs, we identified several receptors whose knockdown significantly reduced the number of dendritic filopodia. Notably, the Down syndrome cell adhesion molecule (Dscam1) and the Eph receptor tyrosine kinase emerged as key regulators in this process. While previous studies suggested the involvement of *Dscam1* in aCC dendritogenesis, our observations revealed that *Dscam1* is not linked to Cdc42 activation, as normal activation occurred in *Dscam1* null

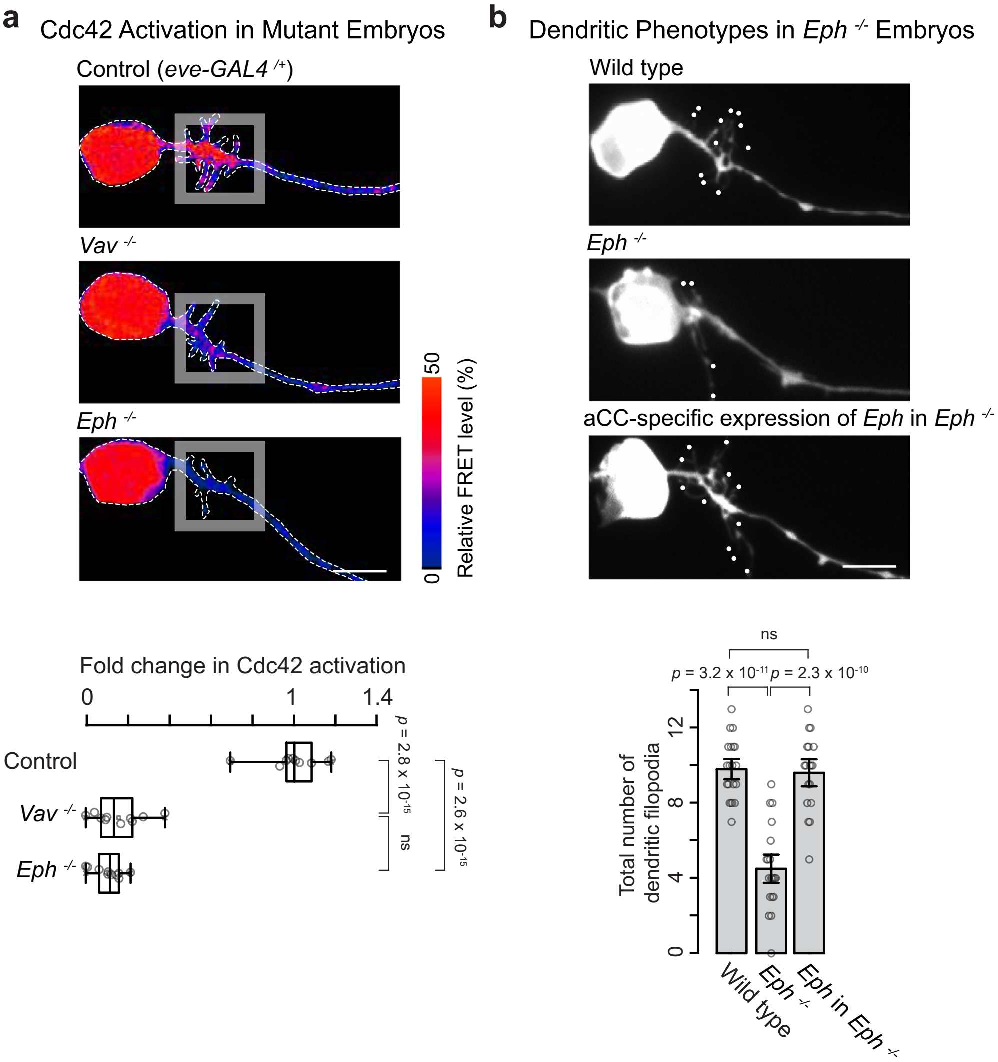

Fig. 2 | Vav and Eph Regulate Cdc42 Activation and Dendritic Filopodia Outgrowth. a Top: Pseudocolor images of aCC motoneurons in control (*eve-GAL4*$^{/+}$), *Vav*$^{-/-}$, and *Eph*$^{-/-}$ embryos at 15:00 AEL, showing aProbe FRET signals, with warmer colors indicating higher Cdc42 activation levels. Dashed lines outline individual neurons. Bottom: Quantification of Cdc42 activation in dendritic filopodia regions is shown below. Statistical analysis was performed by one-way ANOVA ($F_{2,27} = 204$, $p = 0.0$) with Tukey's post hoc tests ($n = 10$ neurons per genotype). Analyses of Cdc42 activation in all other figures are also shown at 15:00 AEL. Box plots show the median (center line), the 25th and 75th percentiles (bounds of box), and the whiskers extend to the minimum and maximum. **b** Top: Representative images of dendritic filopodia outgrowth in wild-type, *Eph*$^{-/-}$, and aCC-specific expression of *Eph* in *Eph* $^{-/-}$ embryos. Bottom: Quantification of dendritic filopodia number is shown below. Statistical analysis was performed by one-way ANOVA ($F_{2,55} = 45$, $p = 2.1 \times 10^{-12}$) with Tukey's post hoc tests (20, 20, and 18 neurons for wt, *Eph* $^{-/-}$, and *Eph* in *Eph* $^{-/-}$, respectively). Error bars represent the mean ± SEM. Scale bars: 5 µm. Source data are provided as a Source Data file.

mutants[52]. This finding shifted our focus to the Eph receptor tyrosine kinase as a potential key regulator of this pathway. To investigate this further, we examined Cdc42 activation patterns in *Eph*^{x652} null mutants (*Eph* $^{-/-}$). The genetic simplicity of *Drosophila*, which contains only a single *Eph* gene[76], allowed us to directly assess the impact of *Eph* disruption on Cdc42 activation. Our results confirmed our hypothesis: in *Eph* $^{-/-}$ mutants, we observed an almost complete absence of Cdc42 activation in the proximal axon (Fig. 2a). This strongly indicates that the Eph receptor plays a critical role in regulating Cdc42 activation during dendritogenesis.

To further validate our findings, we assessed the number of dendritic filopodia in *Eph* $^{-/-}$ mutants, providing a critical validation experiment for our RNAi results. We observed a significant reduction in dendritic filopodia in *Eph* $^{-/-}$ embryos (Fig. 2b), with this decrease comparable to that observed with *Eph* RNAi expression in aCC motoneurons using the *eve-GAL4* driver (5.5 ± 0.5 µm in knockout, 4.1 ± 0.7 µm in knockdown, $p = 0.14$; Welch's *t*-test). Importantly, this reduction in dendritic filopodia was successfully rescued by expressing *Eph* specifically in aCC motoneurons (Fig. 2b). These results suggest that the Eph receptor functions in a cell-autonomous manner to regulate Cdc42 activation and promote aCC dendritogenesis.

The SH2 domain of Vav interacts with the Juxtamembrane Tyrosine residues of Eph

Thus far, we have explored the activation of Cdc42, focusing on the roles of Vav and Eph. While the activation of Cdc42 by Vav and Eph appears to be a novel finding, there is a precedent in mammalian systems where EphA4 and Vav2 have been shown to interact and form a complex that activates Rac1, another small GTPase[77]. This observation led us to hypothesize that *Drosophila* Vav and Eph might interact in a similar manner, but with the specific outcome of activating Cdc42. To investigate this hypothesis, we conducted biochemical assays using the *Drosophila* S2 cell line. We transiently transfected these cells with expression plasmids encoding FLAG-tagged Vav (FLAG-Vav, a construct where the FLAG epitope is fused to *Drosophila* Vav) and Eph-IC-Fc (the intracellular domain of *Drosophila* Eph fused to the human Fc

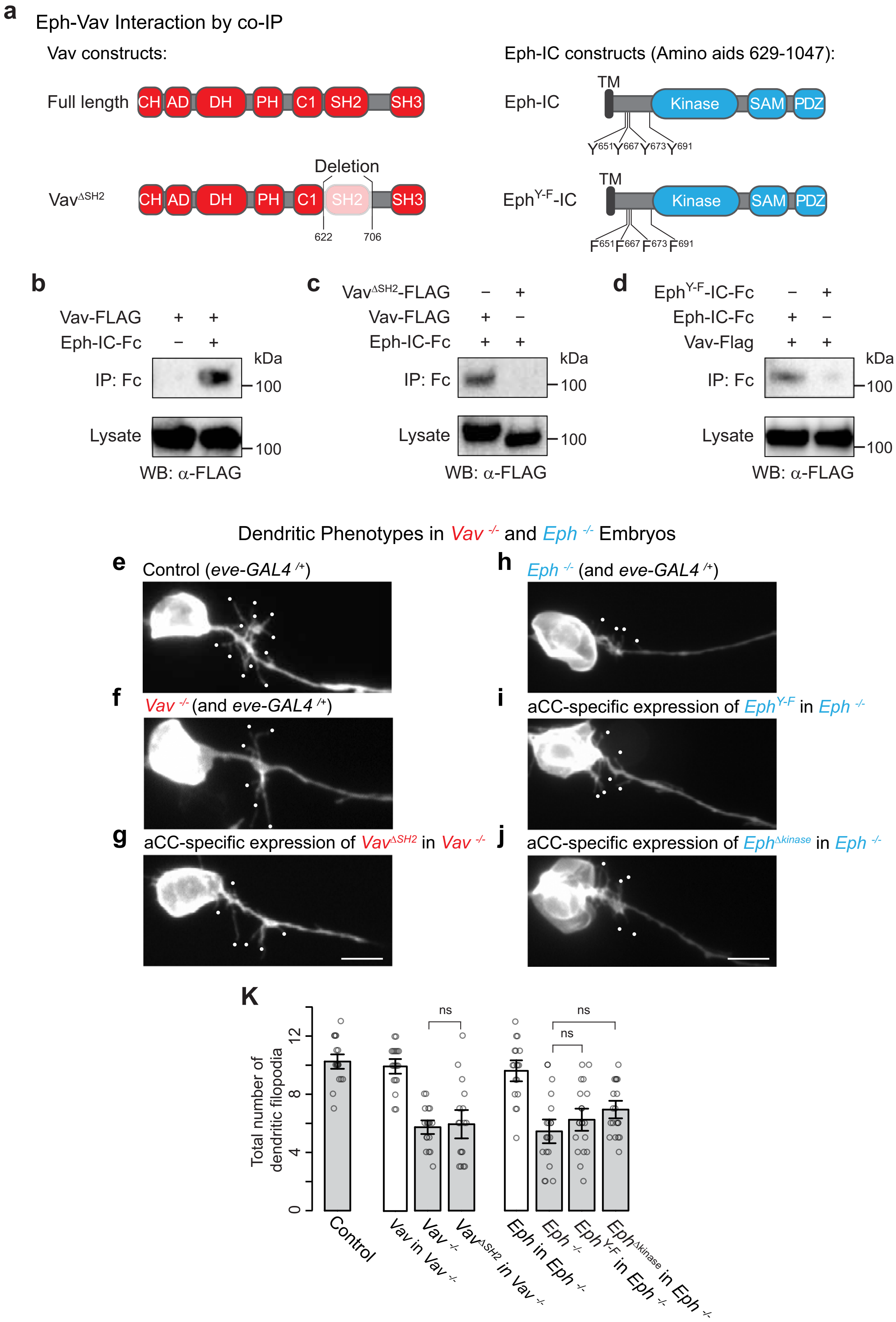
a
Eph-Vav Interaction by co-IP
Vav constructs:
Full length
CH AD DH PH C1 SH2 SH3
Deletion
Vav^ΔSH2
CH AD DH PH C1 SH2 SH3
622 706
Eph-IC constructs (Amino aids 629-1047):
Eph-IC
TM
Kinase SAM PDZ
Y651 Y667 Y673 Y691
Eph^Y-F-IC
TM
Kinase SAM PDZ
F651 F667 F673 F691
b
Vav-FLAG + +
Eph-IC-Fc − +
IP: Fc
Lysate
kDa
100
100
WB: α-FLAG
c
Vav^ΔSH2-FLAG − +
Vav-FLAG + −
Eph-IC-Fc + +
IP: Fc
Lysate
kDa
100
100
WB: α-FLAG
d
Eph^Y-F-IC-Fc − +
Eph-IC-Fc + −
Vav-Flag + +
IP: Fc
Lysate
kDa
100
100
WB: α-FLAG
Dendritic Phenotypes in Vav -/- and Eph -/- Embryos
e
Control (eve-GAL4 /+)
f
Vav -/- (and eve-GAL4 /+)
g
aCC-specific expression of Vav^ΔSH2 in Vav -/-
h
Eph -/- (and eve-GAL4 /+)
i
aCC-specific expression of Eph^Y-F in Eph -/-
j
aCC-specific expression of Eph^Δkinase in Eph -/-
K
Total number of dendritic filopodia
0
4
8
12
ns
ns
ns
Control
Vav in Vav -/-
Vav -/-
Vav^ΔSH2 in Vav -/-
Eph in Eph -/-
Eph -/-
Eph^Y-F in Eph -/-
Eph^Δkinase in Eph -/-

Fig. 3 | Vav SH2 domain and Eph tyrosine residues essential for dendritic outgrowth. a Schematic of Vav and Eph constructs used in co-immunoprecipitation (co-IP) assays, with amino acid positions indicated. TM, transmembrane domain; IC, intracellular domain. Vav$^{\Delta SH2}$ is a mutant lacking the SH2 domain. Eph$^{Y\text{-}F}$ is a phosphorylation-deficient mutant in which key tyrosines in the juxtamembrane region are replaced with phenylalanines. **b–d** Representative Western blots showing co-IP results between Vav-FLAG and Eph-Fc. Vav$^{\Delta SH2}$ and Eph$^{Y\text{-}F}$ were included to assess binding specificity. Vav "IP" denotes immunoprecipitation, and "WB" indicates Western blotting. Comparable results were observed across three independent biological replicates. **e–j** Representative images of dendritic outgrowth under various conditions: control, *Vav*$^{-/-}$, aCC-specific expression of *Vav*$^{\Delta SH2}$ in *Vav*$^{-/-}$, *Eph*$^{-/-}$, aCC-specific expression of *Eph*$^{Y\text{-}F}$, and *Eph*$^{\Delta kinase}$ in *Eph*$^{-/-}$ embryos. **k** Quantification of dendritic filopodia per aCC neuron for the indicated genotypes. Statistical analysis was performed using one-way ANOVA ($F_{2,57} = 2.4$, $p = 0.1$) with Tukey's post hoc tests (20, 19, 19, 18, 18, 20, 20, and 20 neurons for control, *Vav* in *Vav*$^{-/-}$, *Vav*$^{-/-}$, *Vav*$^{\Delta SH2}$ in *Vav*$^{-/-}$, *Eph* in *Eph*$^{-/-}$, *Eph*$^{Y\text{-}F}$ in *Eph*$^{-/-}$, and *Eph*$^{\Delta kinase}$ in *Eph*$^{-/-}$, respectively). The rescue data for *Vav* in *Vav*$^{-/-}$ and *Eph* in *Eph*$^{-/-}$ (white bars) are replotted from Fig. 1b and Fig. 2b, respectively. Error bars represent the mean ± SEM. Scale bars: 5 µm. Source data are provided as a Source Data file.

domain for protein A/G bead interaction) (Fig. 3a). After transfection, we performed immunoprecipitation to isolate the Eph receptors from the cell lysates. The immunoprecipitated proteins were then analyzed via Western blotting to detect potential interactions between Vav and Eph.

Our initial experiment successfully demonstrated the interaction between Vav and Eph (Fig. 3b). Building on this result, we next sought to identify the specific regions of interaction between the two proteins. Given the cross-species conservation of Eph-Vav interactions, we hypothesized that the SH2 domain of Vav binds to phosphorylated tyrosine residues on Eph. To test this, we first examined the role of the SH2 domain in Vav. We generated a Vav deletion mutant lacking the SH2 domain (Vav$^{\Delta SH2}$) (Fig. 3a) and found that this mutant did not interact with Eph (Fig. 3c), underscoring the essential role of the SH2 domain in mediating the interaction. SH2 domains typically bind preferentially to phosphorylated tyrosine residues. Thus, we shifted our focus to the tyrosine residues of Eph, specifically in the juxtamembrane (JM) region, which is known to be autophosphorylated by the receptor's intrinsic kinase activity, as demonstrated in mouse EphA4[77]. In *Drosophila* Eph, this region contains four tyrosines. We substituted them with phenylalanines (Y651F/Y667F/Y673F/Y691F), generating a mutant referred to as Eph$^{Y\text{-}F}$ (Fig. 3a). This commonly used approach blocks phosphorylation while preserving overall protein structure. Vav failed to interact with the Eph$^{Y\text{-}F}$ mutant (Fig. 3d), indicating that phosphorylation at these sites is required for Vav recruitment. In summary, our findings from *Drosophila* S2 cell assays reveal a specific interaction between the JM tyrosines of Eph and the SH2 domain of Vav.

The Eph-Vav interaction promotes dendritic filopodia outgrowth following Eph autophosphorylation

To further investigate the physiological relevance of the interaction between Vav and Eph, we tested the deletion and mutation constructs in vivo. Based on the successful rescue of the loss-of-dendrite phenotype in aCC motoneurons observed with wild-type constructs (Figs. 1b and 2b; summarized in Fig. 3k), we hypothesized that if the interaction sites are essential, these mutant constructs would fail to rescue the phenotype.

First, we specifically expressed *Vav*$^{\Delta SH2}$—the deletion mutant lacking the SH2 domain—in aCC neurons of *Vav*$^{-/-}$ mutants. The expression of *Vav*$^{\Delta SH2}$ failed to rescue the dendritic phenotype (Fig. 3e–g, k). Next, we expressed *Eph*$^{Y\text{-}F}$—a mutant that prevents phosphorylation—in *Eph*$^{-/-}$ mutants. Similar to *Vav*$^{\Delta SH2}$, *Eph*$^{Y\text{-}F}$ expression also failed to rescue the phenotype (Fig. 3h, i, k). These results demonstrate that the phosphorylation-dependent interaction between Vav and Eph is crucial for aCC dendritogenesis.

Since Eph phosphorylation typically depends on its intrinsic tyrosine kinase activity[78,79], we further examined the role of the intracellular tyrosine kinase domain. We generated an Eph deletion mutant lacking this domain (*Eph*$^{\Delta kinase}$) and expressed it in *Eph*$^{-/-}$ mutants. Expression of *Eph*$^{\Delta kinase}$ also failed to rescue the phenotype (Fig. 3j, k). Collectively, our data suggest that the kinase domain of Eph autophosphorylates its juxtamembrane tyrosines, creating docking sites for the SH2 domain of Vav. This phosphorylation event leads to the localization of Vav to the plasma membrane.

Membrane localization of Vav is essential for dendritic filopodia outgrowth

This membrane localization of Vav is potentially crucial for the activation of Cdc42, as Cdc42 typically localizes to the membrane via its CAAX motif. Consequently, Vav would have a higher likelihood of interacting with Cdc42 if it is stably localized on the membrane. To test this hypothesis, we engineered a membrane-anchored version of Vav (myr-Vav$^{DH\text{-}PH}$) by fusing a myristoylation signal to its RhoGEF domain, thereby mimicking the membrane localization of Vav. We then investigated whether this modification could compensate for the absence of Eph. To do so, we expressed the *myr-Vav*$^{DH\text{-}PH}$ construct in *Eph*$^{-/-}$ embryos using the *eve-GAL4* driver. Given the ongoing activity of endogenous Vav, we aimed to maximize the expression of *myr-Vav*$^{DH\text{-}PH}$ by using two copies of the *GAL4* driver. Remarkably, overexpressing *myr-Vav*$^{DH\text{-}PH}$ successfully rescued the *Eph* mutant phenotype (Fig. 4a–c, f). To confirm that this rescue effect was specifically due to the membrane localization of Vav, and not merely an increase in its overall levels, we overexpressed wild-type *Vav*. However, this did not yield a similar rescue (Fig. 4d, f). These findings underscore the critical role of Vav's plasma membrane localization, facilitated by Eph, in driving proper aCC dendritogenesis.

Furthermore, we investigated the necessity of Vav's GEF catalytic activity in this rescue experiment. To do this, we introduced a double-point mutation (L356A, K357A) into the DH domain, which is known to abolish GEF catalytic activity[80]. Significantly, overexpression of this catalytically inactive form (*myr-Vav*$^{DH[AA]\text{-}PH}$) failed to rescue the *Eph* mutant phenotype (Fig. 4e, f). These results strongly suggest that Vav's GEF activity is essential for its role in aCC dendritogenesis.

Vap33 cooperates with Eph to activate Cdc42 during aCC Dendritogenesis

It appears that Eph phosphorylation is a key event in the downstream signaling of Eph. The next question is how Eph becomes phosphorylated. Typically, phosphorylation of Eph receptors is triggered by binding to specific ligands, which in turn dimerize the receptors. In *Drosophila*, *Ephrin* and *Vap33* have been identified as the primary ligands for Eph receptors[76,81,82]. We sought to determine the role of these ligands in dendritic filopodia formation within aCC motoneurons. To explore this, we examined *Ephrin*^{I95} and *Vap33*$^{\Delta 31}$ mutant embryos, which lack their respective proteins. The results of this analysis were quite revealing. We observed a significant reduction in the number of dendritic filopodia in *Vap33*$^{-/-}$ embryos (Fig. 5a), whereas *Ephrin*$^{-/-}$ embryos did not show a substantial difference from wild-type embryos (Supplementary Fig. 5). Importantly, this reduction in filopodia was not due to global changes in the circuit architecture of the VNC, as the neuropiles remained intact (Supplementary Fig. 6).

This distinct phenotype in *Vap33*$^{-/-}$ mutants has directed our research focus towards understanding Vap33's function. To begin, we assessed whether the *Vap33* mutation influences Cdc42 activation. Our analysis revealed that Cdc42 activation is significantly decreased in *Vap33*$^{-/-}$ embryos (Fig. 5b). Notably, the extent of this reduction in Cdc42 activation is comparable to what we observed in *Vav*$^{-/-}$ or *Eph*$^{-/-}$ embryos. Importantly, none of these mutations, including *Vap33*$^{-/-}$, affect Cdc42 activation in the cell body, suggesting that Cdc42

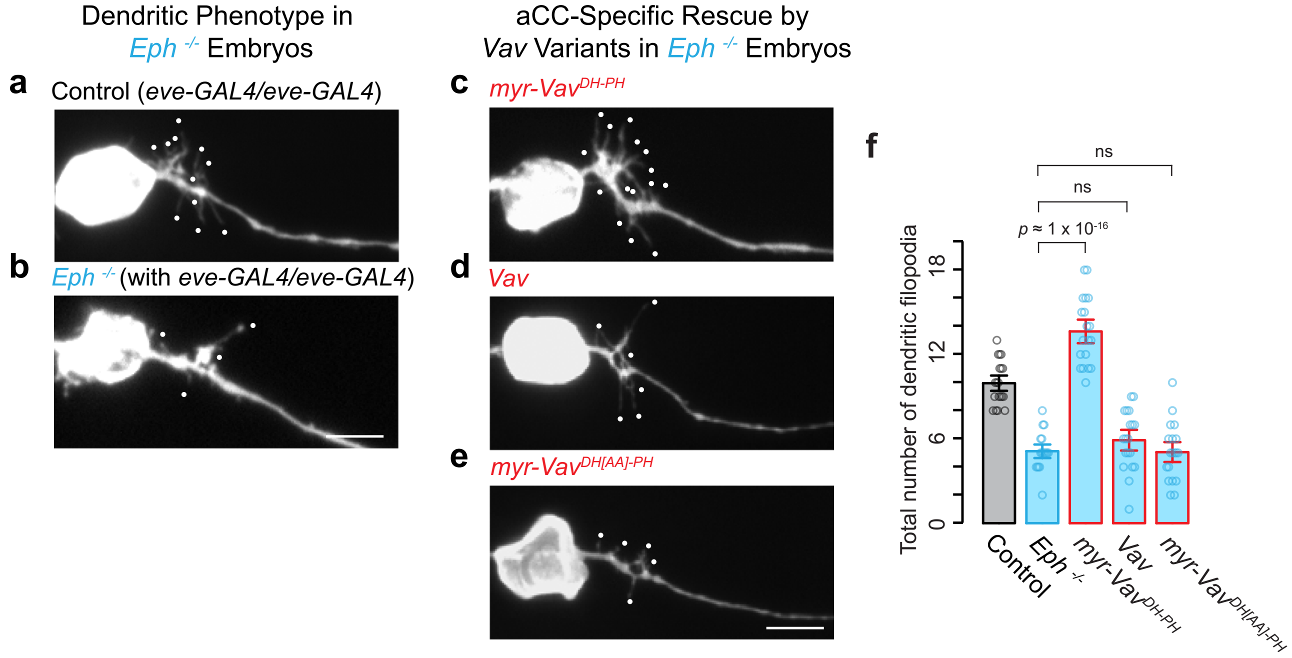

Fig. 4 | Membrane-localized Vav rescues the loss-of-dendritic phenotype in Eph mutants. a–e Representative images showcasing dendritic outgrowth in various experimental setups: control, $Eph^{-/-}$, aCC-specific expression of $myr\text{-}Vav^{DH\text{-}PH}$, *Vav*, and $myr\text{-}Vav^{DH[AA]\text{-}PH}$ in $Eph^{-/-}$ embryos. **f** Quantification of dendritic branches per aCC neuron for the indicated genotypes. Statistical significance was determined using one-way ANOVA ($F_{4,89} = 70$, $p = 0.0$) with Tukey's post hoc tests. The analysis included 19, 18, 19, 19, and 19 neurons for control, $Eph^{-/-}$, $myr\text{-}Vav^{DH\text{-}PH}$ in $Eph^{-/-}$, *Vav* in $Eph^{-/-}$, and $myr\text{-}Vav^{DH[AA]\text{-}PH}$ in $Eph^{-/-}$, respectively. Error bars represent the mean ± SEM. Scale bars: 5 µm. Source data are provided as a Source Data file.

activation is regulated by distinct signaling pathways in the cell body versus the dendrites.

Bellen's lab previously demonstrated that mouse ortholog of Vap33, VAPB, interacts with EphA4 using a co-immunoprecipitation (co-IP) assay[81]. Nevertheless, the interaction between *Drosophila* Vap33 and Eph had not been tested. To this end, we performed a similar co-IP assay. HEK293 cells were transfected with expression constructs encoding V5-Vap33 (V5 being an epitope tag) and Eph-LBD-Fc (the putative ligand-binding domain of Eph fused to the Fc domain). Compared to the negative control (Fc only), Vap33 exhibited binding to Eph-LBD (Fig. 5c). Building on this, we hypothesized that Vap33 and Eph may function within the same signaling pathway during aCC dendritogenesis. To evaluate this, we examined their genetic interaction. Our initial attempt to generate a double homozygous combination was unsuccessful due to the limited availability of genetic tools necessary to combine the *Vap33* and *Eph* genes, located on the X and 4th chromosomes respectively, within the same animals. As an alternative, we tested a double heterozygous combination. Remarkably, these double heterozygous mutants exhibited a subtle but statistically significant reduction in dendritic filopodia formation in aCC motoneurons (Fig. 5d), a reduction not observed in either of the single heterozygous mutants (Fig. 5d). This genetic interaction supports the idea that *Vap33* and *Eph* cooperatively promote dendritic filopodia outgrowth in aCC motoneurons.

aCC dendritic Filopodia outgrowth requires the non-cell-autonomous role of Vap33

Next, we sought to determine the timing and cellular context of Vap33 expression in relation to Eph function during aCC dendritogenesis. Two possible scenarios were considered: (1) Vap33 is expressed within the aCC motoneuron itself, functioning cell-autonomously in conjunction with Eph receptors either in the secretory pathway or at the plasma membrane; or (2) Vap33 is expressed in nearby neurons and exerts its effects on aCC motoneurons through non-cell-autonomous mechanisms. To address this, we analyzed which neurons express Vap33 using recent single-cell RNA sequencing data[83]. By 11:20 AEL (1.5 hours before dendritogenesis begins), Vap33 is expressed in subsets of neurons (Fig. 6, b). To further characterize the identity of these neurons, we compared differentially expressed genes (DEGs) in Vap33-positive clusters with two reference datasets that define neuronal cell types[83,84]. This comparison suggested that Vap33-expressing cells include a broad range of cell types, such as cholinergic neurons, GABAergic neurons, and some neural progenitor cells. To validate these transcriptomic findings, we performed immunostaining on wild-type embryos using available Vap33-specific antibodies. Our observations revealed that Vap33 is present in many, but not all, neurons within the VNC, including aCC, as early as 11:00 AEL (Fig. 6c).

While these findings confirm that Vap33 is broadly expressed, they do not definitively support either of the proposed scenarios. To pinpoint the specific location of its source, we conducted a series of rescue experiments in $Vap33^{-/}$ mutants. We first expressed *Vap33* specifically in aCC motoneurons. This aCC-specific expression did not rescue the mutant phenotype (Fig. 6d). In contrast, when we expressed Vap33 in all neurons except aCC using the pan-neuronal *elav-GAL4* driver combined with the *eve-GAL80* repressor, we successfully rescued the phenotype (Fig. 6e). Interestingly, non-aCC expression of *Vap33* in a wild-type background modestly increased dendritic filopodia (Supplementary Fig. 7). This may be due to elevated *Vap33* dosage or early timing of its expression. Nevertheless, these findings support the idea that Vap33 acts through non-cell-autonomous signaling to promote filopodial outgrowth in aCC motoneurons. To further test this model, we knocked down *Vap33* in a subset of VNC neurons while excluding aCC, using two independent GAL4 drivers—*R12B08-GAL4* and *R13C11-GAL4*—which target distinct neuronal populations. In both cases, partial knockdown of *Vap33* resulted in a significant reduction in dendritic filopodia in aCC neurons (Supplementary Fig. 8). Collectively, these results provide strong evidence that Vap33 is produced by neurons other than aCC and functions non-cell-autonomously, likely serving as a ligand for Eph receptors to regulate dendritic filopodial outgrowth.

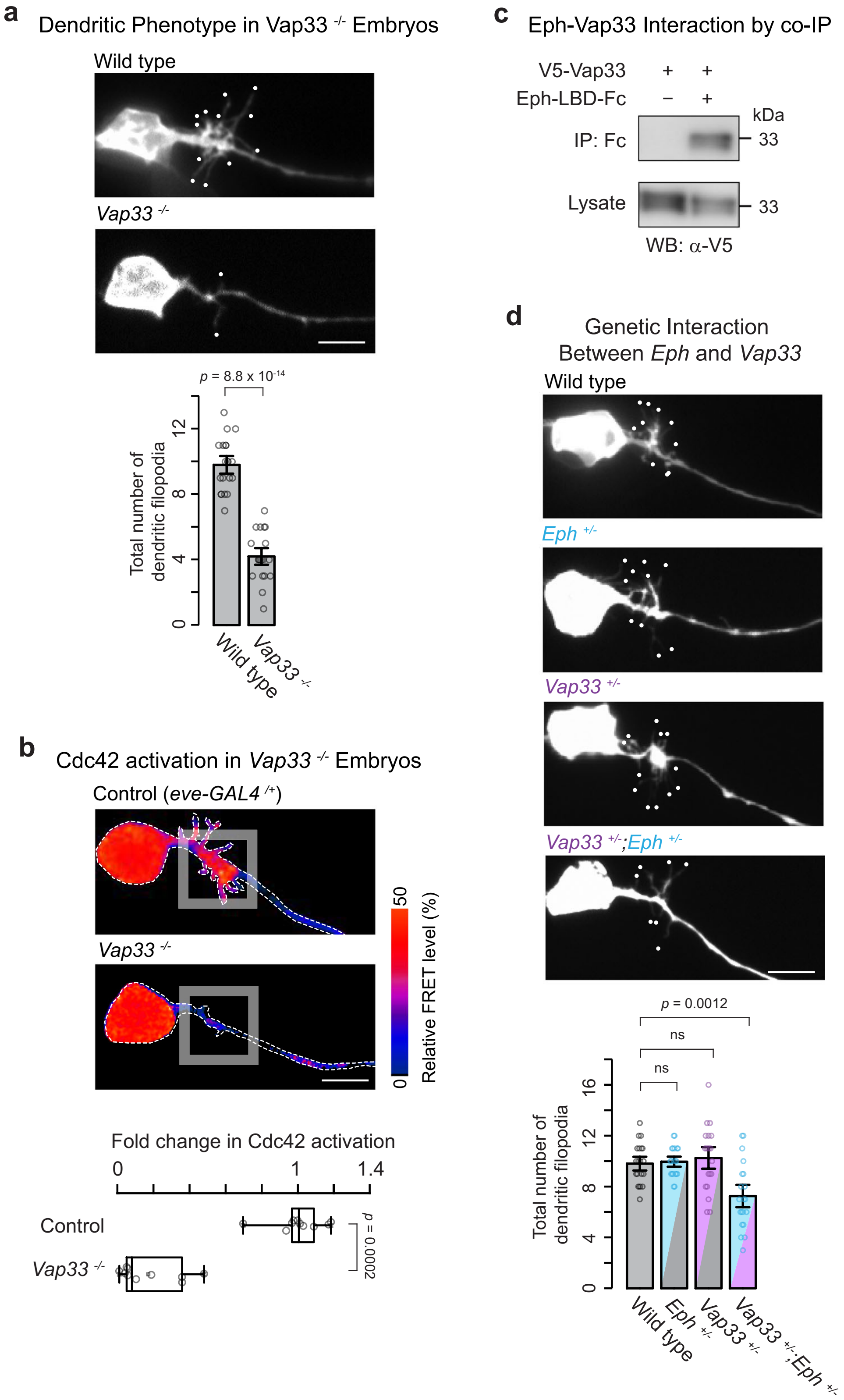

Fig. 5 | Vap33 promotes dendritogenesis and activates Cdc42 via interaction with Eph receptors. a Top: Representative images of dendritic outgrowth in wild-type and *Vap33* $^{-/-}$ embryos. Bottom: Statistical analysis (two-sided Student's *t*-test) shows significant differences ($n = 20$ neurons per genotype). **b** Top: Pseudocolor images showing aProbe responses in control and *Vap33* $^{-/-}$ embryos. Bottom: Quantification of Cdc42 activation levels per aCC neuron indicates significant differences (two-sided Mann–Whitney *U* test, $n = 10$ neurons per genotype). Box plots show the median (center line), interquartile range (box), and minimum–maximum values (whiskers). **c** Western blots showing co-IP between V5-Vap and the Eph ligand-binding domain (LBD)-Fc. The interaction was assessed using cell lysates. Comparable results were observed across three independent biological replicates. **d** Top: Images of dendritic outgrowth in embryos heterozygous for *Eph*, *Vap33*, and double heterozygous for both. Bottom: Dendritic filopodia counts per aCC neuron reveal significant differences (one-way ANOVA, $F_{3,76} = 8.9$, $p = 3.8 \times 10^{-5}$) with Tukey's post hoc tests ($n = 20$ neurons per genotype). Error bars represent the mean ± SEM. Scale bars: 5 µm. Source data are provided as a Source Data file.

Vap33 is a temporal regulator for dendritic filopodia formation in motoneurons

Our final question centers on how the timing of dendritogenesis is determined. Importantly, Vap33 is already expressed by 11:00 AEL (Fig. 6a–c), well before the onset of dendritogenesis. Similarly, Eph, Vav, and Cdc42 are all known to be expressed in the VNC by at least 11:00 AEL[51,71,76]. Thus, the necessary components for dendritogenesis are present early in development. The precise timing may be controlled by regulatory events downstream of protein expression. One intriguing possibility is that Vap33 may start being secreted externally at the onset of dendritogenesis, around 13:00 AEL.

To test this hypothesis, we took two approaches. First, we used a point mutation in Vap33 that is known to disrupt its secretion: Vap33^{P58S}. Using the same rescue strategy as previously shown in Fig. 6e—expressing Vap33^{P58S} in all neurons except aCC—we observed no phenotypic rescue in Vap33 mutants. This contrasts with the robust rescue obtained using wild-type *Vap33* (5.2 ± 0.5 for *Vap33*^{P58S} vs. 8.7 ± 0.8 for wild-type *Vap33*, $p = 0.0023$ by Mann–Whitney *U* test, $n = 17$–18 per genotype). These findings indicate that secretion of Vap33 from non-aCC neurons is essential for its non-cell-autonomous function. Next, we asked whether extracellular Vap33 availability might serve as a time-regulating cue for dendritogenesis. To test this, we performed immunostaining on wild-type embryos without the use of detergents. Unlike typical immunofluorescence, which includes a permeabilization step to detect both intracellular and extracellular components (as shown in Fig. 6c), this method identifies only the extracellular portion of Vap33. The effectiveness of this approach has been demonstrated in a previous study by Tsuda et al.[81]. Using this method, we observed that in the VNC, the fluorescence level of Vap33 earlier than 13:00 AEL is undetectable (Fig. 7a), resembling the signal seen in *Vap33* $^{-/-}$ embryos at 15:00 AEL, which serves as a negative control. Intriguingly, the fluorescence level begins to increase substantially at 13:00 AEL (Fig. 7a), coinciding with the onset of dendritogenesis. This observation strongly supports our hypothesis that Vap33 secretion acts as a timing signal for dendritogenesis.

Furthermore, we observed that subsets of cells in the VNC produce the extracellular portion of Vap33. Extracellular Vap33 is also localized in the neuropiles of the VNC. This distribution suggests that secreted Vap33 is not limited to aCC motoneurons but is likely shared among multiple motoneuron populations, most of which extend their dendrites into the same neuropilar regions as aCC[85]. In *Drosophila* embryos, each hemisegment contains approximately 36 motoneurons, with each typically innervating one of the 30 somatic muscles. During development, these axons exit the VNC via one of five main nerve branches: intersegmental nerve (ISN), ISNb, ISNd, SNa, and SNc. Each motoneuron, depending on its nerve branch, projects its dendrites to specific anteroposterior and mediolateral territories within the VNC[44,86]. To explore this further, we selected four motoneurons from distinct nerve branches with varying birth times and locations: motoneuron 16/15 (MN16/15), raw prawn 3 (RP3), MN24, and RP2 (Fig. 7b). Our observations revealed that dendritic filopodia for these motoneurons begin to emerge at approximately 13:00 AEL and become stabilized by 15:00 AEL (data not shown). In *Vap33* $^{-/-}$ embryos, these motoneurons exhibited a similar degree of dendrite loss as aCC motoneurons at 15:00 AEL (Fig. 7b and Supplementary Fig. 9). Taken together, these findings indicate that Vap33 secretion plays a crucial role in the temporally coordinated outgrowth of dendritic filopodia, contributing to the development of the myotopic map and ultimately influencing the formation of the locomotion circuit.

Discussion

Here, we identify a novel signaling cascade that temporally activates Cdc42 (Supplementary Fig. 10). At the onset of dendritogenesis, Vap33 becomes exposed to the extracellular space, potentially allowing it to bind Eph receptors. This interaction triggers the membrane localization of Vav, which in turn leads to the timely activation of Cdc42. Notably, recent evidence suggests that dysfunction of VAPB, the human ortholog of Vap33, is linked to the progression of ALS8 (see further discussion below). Our findings provide new insights into how VAPB signaling influences the formation of motor circuitry, shedding light on its role in both normal development and disease processes in humans.

In this study, we reveal a previously uncharacterized function of the Rho family guanine nucleotide exchange factor Vav in *Drosophila*. Our findings suggest that Vav serves as a crucial molecular hub, linking Eph receptor activity to Cdc42-dependent dendritic outgrowth. The key evidence supporting this linkage includes: (1) Disruption of either Eph or Vav function leads to similar dendritic outgrowth defects (Figs. 1 and 2). (2) Mutations in either Vav or Eph result in abolished Cdc42 activation (Fig. 2). (3) Vav interacts directly with the Eph receptor (Fig. 3). (4) The interaction domains within Vav and Eph are essential for their role in dendritic development (Fig. 3). (5) Expression of a membrane-tethered version of Vav rescues dendritic growth defects in Eph mutants, while a version of Vav lacking GEF activity does not (Fig. 4). These observations suggest a defined signaling cascade (Supplementary Fig. 10, **Bottom**): Eph receptor activation initiates a critical process by autophosphorylating its tyrosine-rich juxtamembrane region. This phosphorylation enables the SH2 domain of Vav to bind to the phosphorylated tyrosines, facilitating the recruitment of Vav to the plasma membrane. Membrane localization of Vav is essential for activating Cdc42, which likely drives actin polymerization, promoting the protrusion of dendritic filopodia necessary for dendritic outgrowth. Although this study focuses primarily on genetic and biochemical analyses, future investigations could benefit from using pharmacological modulators to further validate and precisely control the Eph-Vav signaling axis. For instance, small-molecule agonists like Doxazosin and its derivatives—which target the ligand-binding domains of Eph receptors and promote receptor phosphorylation[87,88]—could be applied to confirm the pathway's functional relevance and dissect downstream signaling events, including Cdc42 activation via Vav.

Eph-Vav signaling, initially discovered in the context of axon guidance in mouse retinal ganglion cells (RGCs), highlights the pivotal role of Vav2 in activating Rac1[77]. This Rac1 activation is crucial for growth cone repulsion, affecting both plasma membrane internalization and actin cytoskeleton contractility. In *Drosophila*, the genome encodes three Rac genes (*Rac1*, *Rac2*, and *Mtl*) and a single Cdc42 gene[89–91]. Given the high amino acid similarity among these GTPases, it is plausible that all could be activated by Vav. This raises a critical question: How does Vav selectively activate Cdc42, or other GTPases? A potential explanation involves the developmental regulation of gene expression. Our analysis of available scRNA-seq data reveals differential expressions of these GTPases in aCC motoneurons (Supplementary Fig. 11). Between 10:20 and 11:20 AEL, *Cdc42* is expressed at levels similar to *Rac1*, while *Rac2* and *Mtl* are less abundant. During this developmental window, Vav may activate both Cdc42 and Rac1. However, it is noteworthy that our previous findings showed no defects in aCC dendritogenesis in *Rac* triple mutants, though axon guidance was affected in these mutants[52,92]. These observations suggest an additional layer of regulation for Vav, potentially activating Cdc42 or Rac1 in different subcellular locations, thereby leading to distinct downstream signaling pathways. This spatial regulation could result in specific patterns of actin cytoskeletal rearrangements, influencing neuronal morphology in diverse ways.

While *Cdc42* null mutants are embryonic lethal, null mutations in *Vav* and *Eph* do not result in early lethality[71,76,93]. Most *Vav* mutants survive until the pupal stage, although occasional male escapers reach adulthood due to the X-linked inheritance of Vav[71]. *Eph* null mutants are viable into adulthood, though their survival frequency has not been systematically quantified. In contrast, hypomorphic *Eph* alleles exhibit

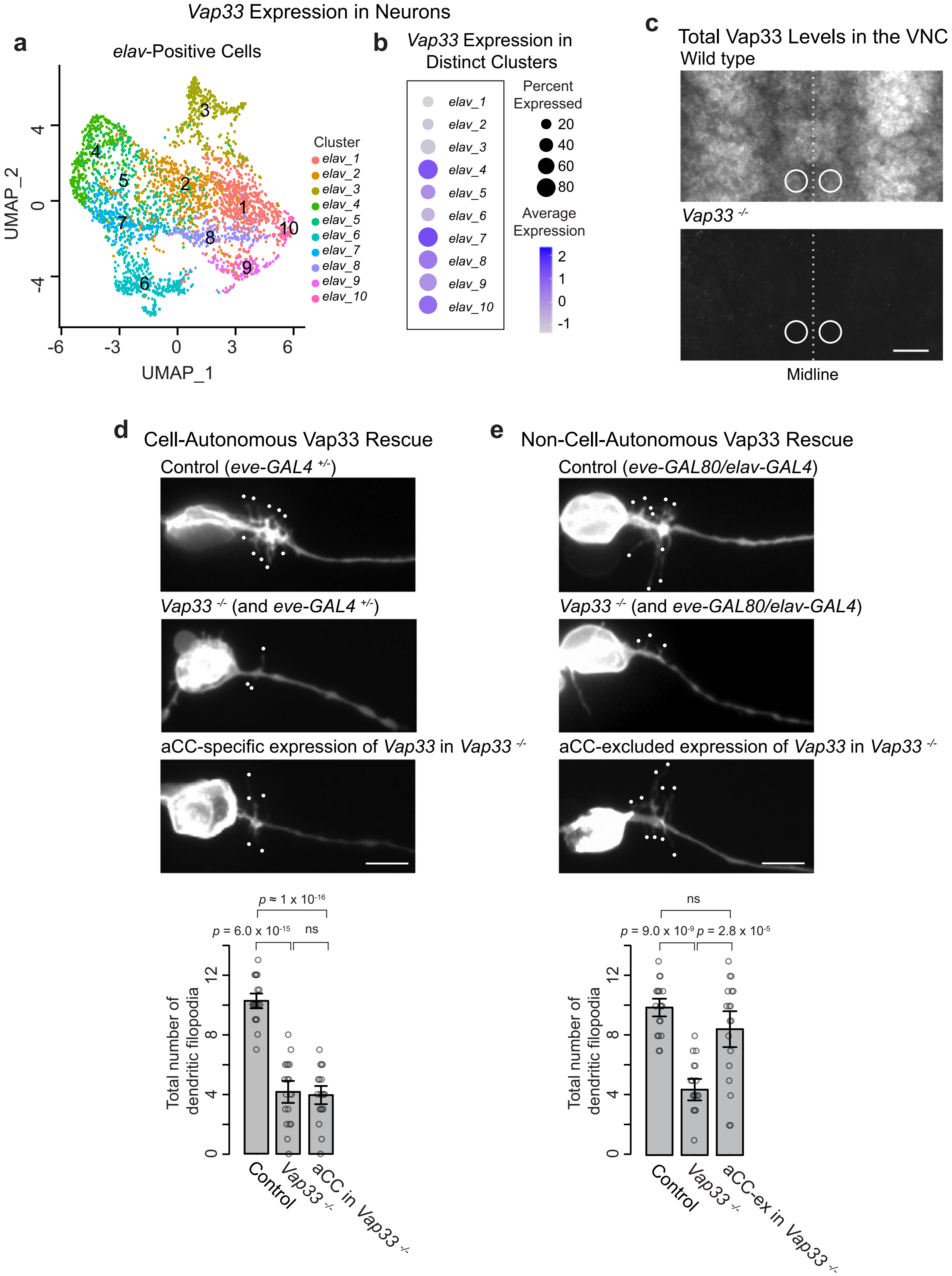

Fig. 6 | Extracellular Vap33 is required for aCC dendritogenesis. a UMAP analysis of embryos (7:20-11:20 AEL) showing *elav*-positive neuronal cells forming 10 clusters, color-coded by defined subsets. **b** Dot plot from scRNA-seq data showing *Vap33* expression across the 10 clusters (data from Seroka et al.). **c** Anti-Vap33 staining in single ventral nerve cord (VNC) segments of wild-type and *Vap33*$^{-/-}$ embryos at 11:00 AEL. Circles indicate aCC motoneuron cell bodies. Similar observations were made in at least three embryos per genotype. **d**, **e** Top: Images of dendritic filopodia in control, *Vap33*$^{-/-}$, and *Vap33*$^{-/-}$ embryos with aCC-specific or aCC-excluded expression of *Vap33*. Bottom: Quantification of dendritic filopodia per aCC neuron reveals significant differences (one-way ANOVA, $F_{2,55} = 76$, $p = 1.1 \times 10^{-16}$) with Tukey's post hoc tests (20, 19, and 19 neurons for control, *Vap33*$^{-/-}$, aCC in *Vap33*$^{-/-}$ in (**d**);, 19, 18, and 18 neurons for control, *Vap33*$^{-/-}$, aCC-ex in *Vap33*$^{-/-}$ in (**e**)). Error bars represent the mean ± SEM. Scale bars: 10 μm in (**c**); 5 μm in (**d**, **e**). Source data are provided as a Source Data file.

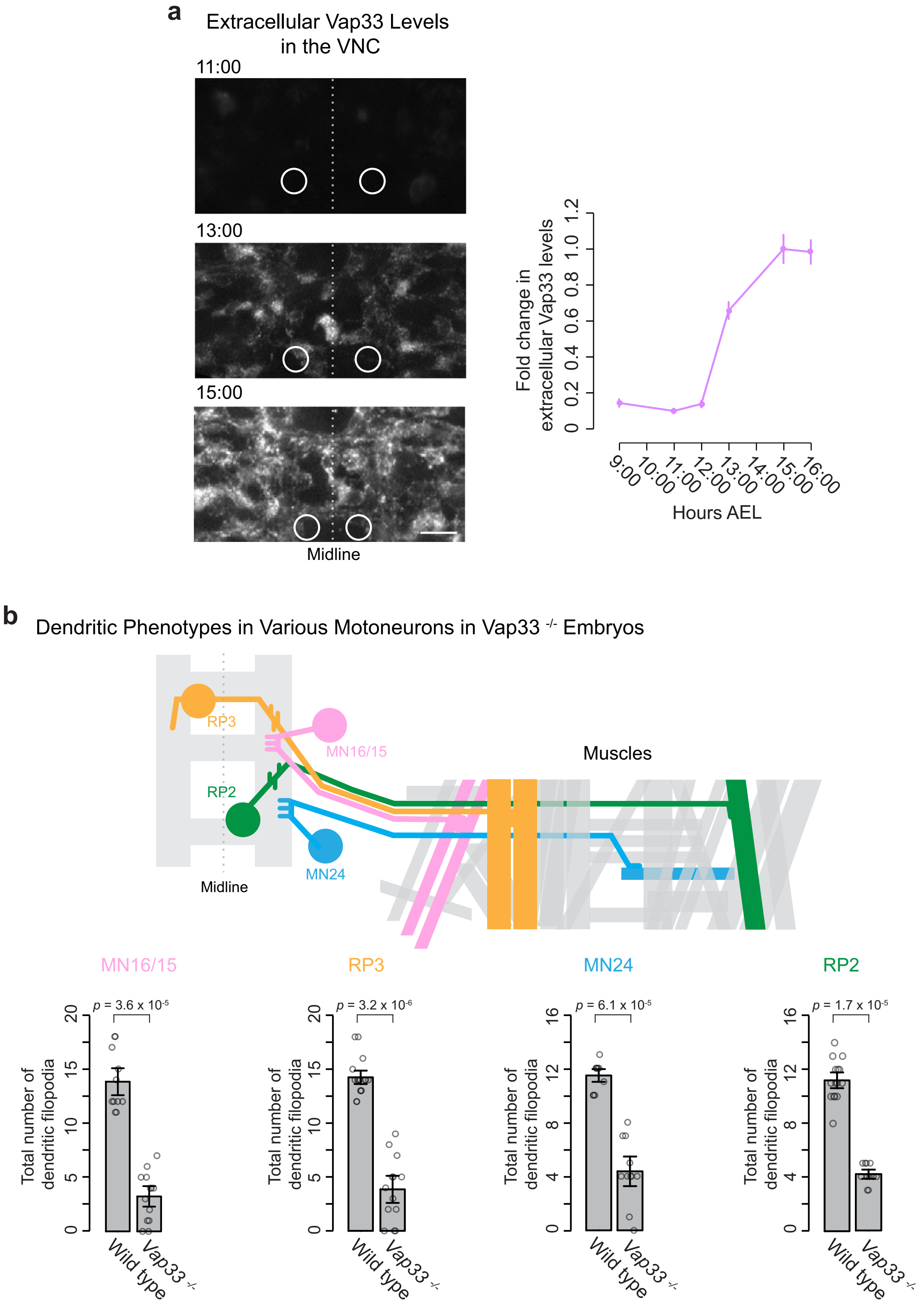

Fig. 7 | Extracellular Vap33 influences global dendritogenesis of motoneurons. Left: Anti-Vap33 staining in wild-type embryos at three developmental time points (11:00, 13:00, and 15:00 AEL), showing detection of extracellular Vap33 under detergent-free conditions. Circles indicate the cell bodies of aCC motoneurons. Right: Quantification of extracellular Vap33 levels is shown, normalized to wild-type embryos at 15:00 AEL (set to 1). **a** In total, six developmental time points were analyzed, including three additional time points not shown in the images (27, 28, 34, 45, 33, and 43 segments analyzed at 9, 11, 12, 13, 15, and 16 hours AEL from abdominal segments A2-A5). **b** Top: Schematic of four motoneurons (MN16/15, RP3, MN24, PR2) in a single embryonic VNC segment, each projecting to specific target muscles. Bottom: Statistical analysis (two-sided Mann–Whitney *U* test) shows significant differences in dendritogenesis between motoneurons of wild-type and *Vap33* $^{-/-}$ embryos (11 and 13 MN16/15 neurons, 18 and 13 RP3 neurons, 11 and 11 MN24, and 15 and 11 RP2 for wt and *Vap33* $^{-/-}$, respectively). Error bars represent the mean ± SEM. Scale bar: 10 µm. Source data are provided as a Source Data file.

significantly reduced viability, with approximately 50% of animals dying before adulthood[94]. Despite these viability limitations, both *Vav* and *Eph* mutants serve as valuable tools for investigating larval and adult phenotypes in the *Drosophila* nervous system. *Vav* and *Eph* mutants exhibit comparable developmental phenotypes. During larval stages, both show cortical axon guidance defects in the developing optic lobe[71,94]. In adults, central brain abnormalities are also evident[71,76,82]. Locomotor impairments are consistently observed in both mutants. For example, Malartre et al. reported that adult *Vav* mutants often fail to walk or fly properly and exhibit a characteristic shaking phenotype[71]. Some are unable to fully eclose, remaining partially trapped in the pupal case—indicative of impaired motor function. Similarly, previous work from Hodge's group reported that panneuronal expression of *Eph* RNAi reduces adult locomotor performance, as measured by the negative geotaxis (climbing) assay[95]. In line with this, our lab observed that larvae expressing panneuronal *Eph* RNAi appeared sluggish and uncoordinated. Quantitative behavioral analyses revealed a significant reduction in both peristaltic wave frequency and turning behavior compared to controls (Supplementary Fig. 12). These findings raise key questions: Do *Eph* and *Vav* also function together in additional processes, such as axon guidance, synapse formation, or neural circuit assembly, beyond their role in dendritogenesis? Are the observed movement impairments in these mutants due to specific disruptions in motor circuits, or do they reflect more widespread developmental abnormalities in the brain? Exploring these questions will help clarify how *Eph* and *Vav* contribute to brain development and motor behavior.

Vap33/VAPB is evolutionarily conserved, with orthologs present in many species ranging from yeast to flies to humans[96]. It is characterized by a major sperm protein (MSP) domain, a coiled-coil domain, and a transmembrane domain, but lacks an N-terminal signal peptide[97,98]. This structural configuration directs a large portion of the protein into the cytoplasm on the ER membrane, classifying it as a type IV transmembrane protein. VAPB is involved in a wide variety of intracellular functions, including membrane trafficking, the unfolded protein response, microtubule organization, autophagosome formation, and calcium homeostasis[64]. Among these functions, the MSP domain plays a particularly critical role in interorganelle communication. For instance, it binds to FFAT motifs in partner proteins, notably several lipid-transfer proteins at Golgi-ER contact sites, and thereby contributes to the regulation of Golgi lipid composition and membrane dynamics[99–101]. In addition to its intracellular roles, the MSP domain is cleaved and secreted from neurons into the extracellular space, where it binds to cell surface receptors such as Eph, Roundabout (Robo), and Leukocyte-antigen-related (Lar)[81,102]. In *C. elegans* striated muscle, this interaction with Robo and Lar positions mitochondria and modulates their morphology[102]. A similar role for the secreted MSP domain has been observed at the neuromuscular junction in *Drosophila* larvae[81,102]. Despite growing evidence of its non-cell-autonomous functions, the molecular mechanism underlying MSP domain secretion and cleavage remains poorly understood. Our recent studies in cultured *Drosophila* S2 cells have begun to shed light on this process[103]. Unlike type I transmembrane proteins, which contain an N-terminal signal peptide that directs them to the ER lumen for conventional ER-to-Golgi secretion, Vap33 follows an unconventional pathway. In these experiments, Vap33 was transfected into S2 cells, and the cultures were treated with Brefeldin A (BFA), a well-established inhibitor of Golgi-dependent transport. Surprisingly, Vap33 remained detectable on the cell surface following BFA treatment, suggesting that it may traffic via a non-classical, Golgi-independent pathway. After synthesis, Vap33 traffics to the plasma membrane, where it is thought to undergo a process termed "topology inversion," meaning a reversal of the protein's orientation so that domains normally inside the cytoplasm become exposed to the extracellular space. The precise subcellular site of this inversion remains unknown. Following inversion, Vap33 is cleaved by Matrix metalloproteinases 1 and 2 (Mmp1/2), resulting in the release of its MSP domain. We hypothesize that a similar secretion mechanism operates in vivo as well. In our working model (Supplementary Fig. 10), subsets of neurons secrete Vap33 extracellularly at the onset of dendritogenesis. The MSP domain then interacts with Eph receptors on the plasma membranes of aCC motoneurons, triggering the timely formation of dendritic filopodia.

Mutations in VAPB have been causally linked to a familial form of amyotrophic lateral sclerosis (ALS), known as ALS8[104–109]. This familial ALS is a slowly progressive, late-onset dominant form initially identified in a Brazilian family[106]. One of the most studied mutations in ALS8 is the substitution of proline with serine at amino acid position 56 ($\text{VAPB}^{\text{P56S}}$)[106–109]. At a cellular level, this mutation leads to protein aggregation in the endoplasmic reticulum (ER), where mutant VAPB sequesters endogenous VAPB, potentially exerting a dominant-negative effect[110–112]. Consequently, the secretion of functional VAPB is significantly reduced[113]. Even when mutant $\text{VAPB}^{\text{P56S}}$ reaches the extracellular space, it is resistant to proteolytic cleavage of the MSP domain, suggesting impaired signaling capacity[114,115]. Supporting this notion, the MSP domain has been detected in blood and cerebrospinal fluid (CSF) of healthy individuals, but is markedly reduced in patients with sporadic ALS, implicating MSP cleavage and secretion defects in disease etiology[116]. In our study, we demonstrate that Vap33 acts non-cell-autonomously to promote motoneuron dendritogenesis. This conclusion is supported by a comprehensive series of genetic experiments, including targeted knockdown, non-cell-autonomous overexpression, and rescue strategies (Fig. 6e **and** Supplementary Figs 7-8). Notably, Vap33 carrying the P58S mutation (corresponding to the human $\text{VAPB}^{\text{P56S}}$) failed to rescue the dendritic defects in *Vap33* $^{-/-}$ mutants when expressed non-cell-autonomously, whereas wild-type Vap33 did rescue the phenotype. This suggests that dendritogenesis depends on the MSP domain of secreted Vap33. These findings raise the possibility that a similar mechanism may operate in mammals: reduced extracellular VAPB signaling could disrupt the spatiotemporal patterning of dendrites, a critical step in the formation of functional motor circuits. Mammalian motoneurons, like their *Drosophila* counterparts, display subclass-specific dendritic arborization patterns within distinct spinal cord territories[117–119]. Disruption of these developmental processes could compromise synaptic targeting and neural circuit integrity, potentially rendering motoneurons more vulnerable to later degeneration. Understanding how VAPB influences dendritic development and extracellular signaling may provide novel insights into the early stages of ALS pathogenesis. Therapeutic strategies aimed at restoring VAPB secretion or mimicking its extracellular function may help mitigate motoneuron dysfunction and slow disease progression.

We convincingly demonstrate that Cdc42 is activated via Vap33-Eph-Vav signaling at the onset of dendritogenesis. However, we do not address why Cdc42 activation is spatially restricted to the proximal region of axons (e.g., Supplementary Fig. 4). The mechanisms underlying this spatial confinement remain poorly understood. Since secreted Vap33 is uniformly distributed throughout the neuropiles of the VNC, it is likely that this spatial regulation is independent of Vap33. We hypothesize that the localization of Eph receptors may play a critical role in determining the spatial restriction of Cdc42 activation. Previous research has shown that certain guidance receptors can localize to specific regions of axons, such as the proximal or distal segments, independently of direct cell-cell contact[120]. For instance, the guidance receptor Derailed localizes to the proximal region of the longest neurite in single cultured *Drosophila* neurons. Building on these findings, we visualized the localization of Eph in cultured neurons and observed a similar proximal distribution in the longest neurites (Supplementary Fig. 13). This suggests that neurons may have intrinsic mechanisms to direct Eph receptors to specific membrane compartments, which could spatially restrict the downstream activation of Cdc42. While this observation provides valuable insight, it remains to be determined whether this spatial organization is established and maintained in vivo and how it might be regulated.

Methods

Molecular cloning

Complementary DNA sequences of *Vav* and *Eph* (LD25754 and RE61046) (*Drosophila* Gene Collection, BDGP) were PCR amplified and subcloned into *pACUH-superfolderGFP* (*sfGFP*) to generate C-terminal *sfGFP* fusions using the NotI restriction site. The *pACUH-sfGFP* vector includes the *sfGFP* sequence in *pACUH* (Addgene) at the NotI and XbaI sites. To create deletion constructs ($Vav^{\Delta SH2}$ and $Eph^{\Delta kinase}$), we performed site-directed mutagenesis using the Q5 Site-Directed Mutagenesis Kit (New England Biolabs). We deleted a DNA sequence encoding the SH2 domain of Vav (amino acids 622-706) or the kinase domain of Eph (amino acids 692-950) from *pACUH-Vav-sfGFP* or *pACUH-Eph-sfGFP*, respectively. To replace tyrosine (Y) with phenylalanine (F), we designed two pairs of mutagenesis primers. We performed two rounds of mutation reactions and introduced four Y-to-F substitutions to the juxtamembrane region of Eph. A synthesized DNA fragment (Integrated DNA Technologies) containing either $myr\text{-}Vav^{GEF\text{-}PH}$ or $myr\text{-}Vav^{GEF[AA]\text{-}PH}$ was cloned into the EcoRI and NotI sites of *pACUH-sfGFP*. Those $\mathrm{Vav}^{\mathrm{GEF\text{-}PH}}$ constructs comprise a GEF-PH domain only (amino acids 220-541).

For co-immunoprecipitation (co-IP) assays in *Drosophila* S2 cells, we designed *pACUH* plasmids to produce FLAG-tagged or Fc-tagged proteins. *Vav-3xFLAG* and $Vav^{\Delta SH2}$*-3xFLAG* fragments were PCR amplified from *pACUH-vav-sfGFP* and *pACUH-*$Vav^{\Delta SH2}$*-sfGFP*. Then, we introduced each fragment to the *pACUH* vector through the NotI and XbaI sites, constructing *pACUH-Vav-3xFLAG* and *pACUH-*$Vav^{\Delta SH2}$ *–3xFLAG*. Human *Fc* fragments were PCR amplified from the *pIB-Fc* vector (a gift from Thomas Kidd). *Eph-IC* and $Eph^{Y\text{-}F}$*-IC* were generated via PCR from the full-length *Eph* and $Eph^{Y\text{-}F}$. *Eph-IC-Fc* and $Eph^{Y\text{-}F}$*-IC-Fc* were assembled into *Not*I- and *Xba*I-digested *pACUH*. *Eph-IC* encodes a fragment of the C-terminal region (amino acids 629-1047). Similarly, for co-IP assays in human HEK293T cells, we designed *pcDNA3.1* plasmids to produce V5-tagged or Fc-tagged proteins. The *Eph ligand-binding domain (LBD)-FLAG-Fc* fragment was amplified from *Eph* cDNA using primers containing a *FLAG* sequence. The *Fc* region was amplified independently. These fragments were assembled into the BamHI and XbaI sites of *pcDNA3.1*. Note that Eph-LBD encodes a fragment of the N-terminal region (amino acids 1-355). The *V5-Vap33* fragment was PCR-amplified from *Vap33* cDNA (previously described[103]) using primers containing a V5 sequence and cloned into the BamHI and XbaI sites of *pcDNA3.1*.

Standard subcloning, PCR amplification (PrimeSTAR Max polymerase, Takara Bio USA), and In-Fusion cloning (In-Fusion Snap Assembly Master Mix, Takara Bio USA) were used to generate all plasmids and intermediates. The oligonucleotides and gene fragments used are listed in Supplementary Table 2.

Transgenic line production

After being sequenced, all plasmids were injected into *attP* embryos expressing *ΦC31* by Rainbow Transgenic Flies and Best Gene.

Fly Stock

Standard *Drosophila* genetic techniques were used for all crosses. All flies were raised at 25 °C. The following lines were obtained from the Bloomington *Drosophila* Stock Center: *eve-GAL4* (BDSC stock no. 7470 and 7473), *elav-GAL4* (8760), *R12B08-GAL4* (48489), *R13C11-GAL4* (48556), *UAS-sif RNAi* (61934), *UAS-Ziz RNAi* (54817), *UAS-RhoGEF3 RNAi* (42526), *UAS-Rtgef RNAi* (32947), *UAS-RhoGEF4 RNAi* (42550), *UAS-pbl RNAi* (36841), *UAS-Cdep RNAi* (31168), *UAS-PsGEF RNAi* (44061), *UAS-GEFmeso RNAi* (42545), *UAS-trio RNAi* (43549), *UAS-unc-89 RNAi* (34000), *UAS-RhoGEF64C RNAi* (31130), *UAS-Pura RNAi* (58270), *UAS-Zir RNAi* (53946), *UAS-spg RNAi* (35396), *UAS-Exn RNAi* (33373),*UAS-Vav RNAi* (39059), *UAS-RhoGEF2 RNAi* (34643), *UAS-Eph RNAi* (60006), *UAS-Vap33 RNAi* (77440), *UAS-mito-HA-GFP* (8442), and *UAS-FLAG-Vap33-HA* (39682). Vav^{2} and Vav^{3} mutants were provided by Dr. Marianne Malartre, The French National Centre for Scientific Research, France. $Vap33^{\Delta 31}$ mutant was obtained from Drs. Hiroshi Tsuda and Hugo Bellen. Some of the lines used in this study were previously generated by our team: *UAS-aProbe*, *UAS-*$aProbe^{dominant\ negative}$, *eve-GAL80*, *UAS-FLAG-*$Vap33^{P58S}$*-HA*, and Eph^{myc}. The genotypes used in each experiment are listed in Supplementary Table 1.

Primary neuronal culture

Flies were allowed to lay eggs on a grape agar plate overnight in a cage. The following day, the collected eggs were dechorionated in a 50% bleach solution for 5 minutes. After dechorionation, the eggs were gathered using a cell strainer (Corning) and gently transferred into SFX culture medium (Hyclone) in a new centrifuge tube using a pen brush. The embryos were mechanically dissociated by homogenization with a plastic homogenizer (Thermo Fisher Scientific), applying 10-20 strokes. To facilitate further dissociation, trypsin was added to the homogenate, and the samples were incubated at 37 °C for 30 minutes. After incubation, 100 µL of fetal bovine serum (FBS; R&D Systems) was added to inhibit the trypsin activity. The mixture was centrifuged at 1,000 rpm for 2 minutes, and the supernatant was carefully removed. The resulting pellet was resuspended in SFX medium supplemented with penicillin/streptomycin (Corning), FBS, and insulin (MilliporeSigma). Finally, the cells were transferred into an 8-well chamber slide (Nunc Lab-Tek) for immunostaining.

Immunohistochemistry

Dissected embryos. Dissected embryos were fixed with 4% paraformaldehyde in phosphate-buffered saline (PBS) for 10 minutes, washed in TBS (0.1% Triton X-100 in PBS), blocked in 10% bovine serum in TBS for 1 hour, and incubated with primary antibodies overnight at 4 °C. The primary antibodies used included rabbit anti-Vap33 (a gift from Hiroshi Tsuda and Hugo Bellen; 1:10,000), mouse anti-Fasciclin II (Developmental Studies Hybridoma Bank; 1:100), and Alexa647-conjugated goat anti-HRP (Jackson ImmunoResearch Labs; 1:500). After washing, embryos were incubated with secondary antibodies conjugated to fluorescent dyes (Thermo Fisher Scientific; 1:500) for 2 hours at room temperature. Following extensive washes with TBS, embryos were mounted in 50% glycerol for slide preparation and imaged using a confocal microscope.

Detection of extracellular Vap33. This protocol is based on the extracellular detection method for Vap33 described by Tsuda et al., with the following modifications. Embryos were processed without detergents, substituting PBS for TBS, and incubated with a rabbit anti-Vap33 antibody (1:500) developed in our recent studies[103], along with an anti-HRP antibody for normalization purposes. All other conditions, including incubation duration and secondary antibody concentration, were maintained as described in the standard staining procedures above.

Primary neurons. Primary neurons were stained using a protocol similar to that for dissected embryos, but neurons were incubated with the secondary antibody for 1 hour at room temperature. We used anti-myc antibody (Developmental Studies Hybridoma Bank; 1:100). After staining, the neurons were submerged in PBS for imaging with a confocal microscope.

Fluorescence Imaging

Fluorescence images were acquired using an inverted microscope (Ti-E, Nikon) equipped with a 100×, 1.45 NA oil immersion objective (Plan

Apo, Nikon). The microscope was connected to a Dragonfly spinning disk confocal unit (CR-DFLY-501, Oxford Instruments). Three excitation lasers (488 nm, 561 nm, and 642 nm) were coupled to a multimode fiber passing through an Andor Borealis unit. A dichroic mirror (Dragonfly laser dichroic for 405/488/561/640 nm) and three bandpass filters (525/50 nm, 600/50 nm, and 725/40 nm) were placed in the imaging path. Images were recorded using an electron-multiplying charge-coupled device camera (Andor iXon, Oxford Instruments) controlled with Fusion software (Oxford Instruments).

For aCC imaging, optical sections with a thickness of 0.5 µm were acquired, spanning a z-depth of 8 µm from the surface of the ventral nerve cord (VNC), where aCC motoneurons are typically located. For VNC imaging, we imaged the entire VNC at 1 µm intervals throughout the z-axis. These images were reconstructed using ImageJ software from the National Institutes of Health (NIH). To maintain consistency, uniform laser power, gain, and exposure time settings were used during data collection. The figures display the resulting images as average intensity projections.

Cell culture and transfection

Drosophila S2R+ cells were maintained in SFX-INSECT culture medium (Hyclone) at 25 °C. Cells were transfected with 300 ng of *pACUH* constructs using 2.5 µL of Effectene (Qiagen). To induce expression in transiently transfected cells, 300 ng of *pAC-GAL4* (Addgene) was co-transfected. Transfections were carried out in 24-well plates. The cells were analyzed 48 hours post-transfection.

HEK293T cells were cultured in Dulbecco's Modified Eagle Medium (HyClone) supplemented with 10% fetal bovine serum (Atlanta Biologicals) in a humidified incubator at 37 °C with 5% CO_2. For transient transfection, cells were seeded into T25 flasks and transfected with 3000 ng of *pcDNA3.1-Eph-LBD-FLAG-Fc* and 200 ng of *pcDNA3.1-V5-Vap33* using polyethylenimine (PEI; Polysciences). Cells were incubated for 3 days post-transfection prior to subsequent analysis.

Co-immunoprecipitation assay

S2 cells or HEK293 cells were lysed in 450 µL of 1% NP-40 lysis buffer or 1 mL of 0.5% NP-40 lysis buffer, respectively. Lysates were incubated with 5 µL of Pierce Protein A/G Magnetic Beads (Thermo Fisher Scientific) overnight at 4 °C with continuous rotation. The beads were washed three times with PBS and eluted with SDS loading buffer. Samples were subjected to SDS-PAGE using a 4-20% polyacrylamide gel (Bio-Rad), followed by protein transfer onto PVDF membranes (Thermo Fisher Scientific). The membranes were blocked at room temperature for 1 hour in 4% skimmed milk in TBS-T (0.1% Tween-20 in TBS) and probed with mouse anti-FLAG antibody (MilliporeSigma; 1:1,000 dilution) or mouse anti-V5 antibody (Thermo Fisher Scientifc; 1:1000 dilution). Anti-mouse secondary antibodies conjugated to horseradish peroxidase (Thermo Fisher Scientific) were used at a dilution of 1:2,000 for 1 hour at room temperature. Blots were developed with a chemiluminescent substrate (Syngene) and imaged using the ChemiDoc Imaging System (Bio-Rad).

Single-cell RNA sequencing data analysis

Single-cell RNA sequencing data were obtained from the NCBI Gene Expression Omnibus (GEO) under accession number GSE202987. Analysis was conducted using R scripts sourced from GitHub (https://github.com/AustinSeroka/2022-Doe-Drosophila-Embryo-Atlas). We employed the Seurat package (v3.1.2) in R, following standard protocols for quality control, data normalization, and analytical procedures. Cells were selected based on mitochondrial gene expression, retaining those with less than 20% mitochondrial reads for further analysis. The *sctransform* tool was used for data normalization to mitigate technical variance. Subsequent filtering and sub-clustering of the central nervous system (CNS) dataset were based on the expression of established neuronal markers, such as *elav*. Clusters were identified using a non-biased approach according to gene expression profiles. Gene expression levels are reported as normalized counts and categorized by developmental stage.

To identify neuron types, we compared the top differentially expressed genes in *Vap33*-positive clusters with published gene signatures from well-characterized neuronal and non-neuronal cell types in the *Drosophila* larval and adult brain[83,84]. These reference profiles included cholinergic, glutamatergic, GABAergic, and peptidergic neurons, as well as neural progenitors, glia, and undifferentiated neuronal precursors.

Motoneuron labeling and imaging

To assess dendritic filopodia in aCC motoneurons, we performed targeted labeling using a lipophilic dye, focusing on four neurons within the A2-5 segments per embryo[69]. Although labeling efficiency varied due to the challenging injection process, typically 2-3 neurons per embryo were successfully labeled and included in the quantification. Embryos were collected at 15:00 AEL, a time point selected because dendritic filopodia have stabilized and maintain a consistent number, facilitating reliable genotype comparisons. To ensure that developmental timing was not altered by the mutations under study, we also examined embryonic gut morphology as an independent developmental marker prior to dissection. Across all genotypes, gut morphology appeared comparable, indicating that overall developmental timing was not affected.

Quantification of dendritic filopodia

We quantified ipsilateral dendritic filopodia extending more than 1 µm along the axon shafts of labeled aCC motoneurons at 15:00 AEL. This time point was chosen because, unlike the dynamic branching observed at 13:00 AEL, the number of filopodia stabilizes, allowing for consistent comparisons across genotypes. Dendritic filopodia were counted using high-resolution confocal microscopy images, and the data were used to compare different genotypes.

FRET imaging and analysis

Fluorescence resonance energy transfer (FRET) data were acquired to measure Cdc42 activation in the proximal axon region of aCC motoneurons at 15:00 AEL. Imaging was performed using an upright Axio Imager Z2 microscope (Carl Zeiss) equipped with a 63× 1.4 NA oil immersion objective (Plan Apo, Carl Zeiss) and an LSM 880 scanning head with a 32-channel GaAsP spectral photomultiplier tube detector. The 458 nm line of an argon laser was used for excitation with the main beam splitter MBS-458/514. Emitted light was detected using two emission filters: 454-518 nm for cyan fluorescent protein (CFP) and 517–605 nm for yellow fluorescent protein (YFP). Image capture was controlled using Zen software (Carl Zeiss).

Raw images were processed by subtracting background fluorescence intensity from non-labeled cells to correct for background noise. Yellow/cyan emission ratios were calculated to generate "FRET images," representing Cdc42 activation levels.

Quantification of Cdc42 activation

To quantify Cdc42 activation along aCC axons, FRET images underwent threshold segmentation to distinguish "object" pixels (representing aCC motoneurons) from "background," based on predefined thresholds. This segmentation was applied across multiple z-planes captured for each neuron. The total yellow/cyan (Y/C) ratio values across all planes were divided by the volume to generate two-dimensional (2D) density maps (Supplementary Fig. 2b, top). From these maps, bar graphs were generated.

For detailed analysis, 30 µm-long lines perpendicular to the midline were drawn on each 2D density map. Values along these lines were averaged and plotted as line charts to represent the Y/C ratio over distance from the cell body (Supplementary Fig. 3b, bottom). To account for variations in protein expression among neurons, values were normalized based on the average Y/C ratio at the cell body (peak) and the axon shaft (baseline, located 20–25 µm from the cell body). Each line plot was fitted with a Gaussian equation, and the area under the curve was calculated to estimate the relative level of Cdc42 activation. This analysis was performed on 10 neurons per genotype, and the resulting values were averaged. Comparisons across genotypes or time points were presented as fold changes.

Quantification of extracellular Vap33

We quantified the relative levels of extracellular Vap33 across developmental stages from 9:00 to 16:00 AEL. Following immunostaining with anti-Vap33 and anti-HRP antibodies, we acquired confocal z-stacks covering the entire VNC. HRP staining was used as an internal control to normalize variability in antibody penetration. To quantify extracellular Vap33, we focused on neuropil regions where motoneuron dendrites form, spanning a 10 µm z-depth centered on this area. Within each VNC segment, we measured the average Vap33 fluorescence intensity and subtracted background levels determined from adjacent non-VNC regions. To correct for slide-to-slide differences in antibody penetration, we used HRP signal intensity from the same segment's longitudinal connectives as a correction factor. This normalization allowed accurate comparison of Vap33 levels across developmental stages.

Behavioral analysis of larvae expressing *Eph* RNAi

UAS-Eph RNAi males and e*lav-GAL4* virgin females, or Oregon-R males and *elav-GAL4* virgin females (control), were crossed in collection cages. Embryos were collected on grape juice agar plates, which were replaced every 2–3 hours to synchronize developmental stages. Embryos at the synthesium stage were selected and incubated at 16 °C for two days. Freshly hatched first instar larvae (<30 minutes old) were transferred to agar plates and allowed to acclimate for 1 minute before recording. Larval behavior was captured using a Nikon dissection microscope equipped with a video camera for 1.5 minutes. The videos were analyzed to quantify the number of full-body peristaltic waves and turns.

Statistical analysis

Statistical analyses were performed using OriginPro (OriginLab). Depending on data distribution, we applied Student's *t*-test, Welch's *t*-test, or the Mann–Whitney *U* test for pairwise comparisons. For multiple comparisons, one-way ANOVA followed by Tukey's post hoc test was used. Sample sizes for FRET analyses and filopodia counting were determined based on preliminary experiments and existing literature to ensure reproducibility. A power analysis, using standard deviations from preliminary data, indicated that a sample size of $n = 11$ neurons for dendrite counts and $n = 10$ neurons for distribution analysis would detect differences with 90% power at a 95% confidence level. Specific statistical tests used and sample sizes for each experiment are provided in the figure legends.

Reporting summary

Further information on research design is available in the Nature Portfolio Reporting Summary linked to this article.

Data availability

All plasmids and transgenic fly lines generated in this study have been deposited at Addgene and the Bloomington Drosophila Stock Center. All datasets necessary for interpretation, verification, and extension of the research are provided in the Source Data file accompanying this paper. Source data are provided with this paper.

References

1. Williams, M. E., de Wit, J. & Ghosh, A. Molecular mechanisms of synaptic specificity in developing neural circuits. *Neuron* **68**, 9–18 (2010).
2. Shen, K. & Scheiffele, P. Genetics and cell biology of building specific synaptic connectivity. *Annu. Rev. Neurosci.* **33**, 473–507 (2010).
3. Yogev, S. & Shen, K. Cellular and molecular mechanisms of synaptic specificity. *Annu. Rev. Cell Dev. Biol.* **30**, 417–437 (2014).
4. Luo, L. Architectures of neuronal circuits. *Science* **373**, eabg7285 (2021).
5. Udin, S. B. & Fawcett, J. W. Formation of topographic maps. *Annu. Rev. Neurosci.* **11**, 289–327 (1988).
6. Inan, M. & Crair, M. C. Development of cortical maps: perspectives from the barrel cortex. *Neuroscientist* **13**, 49–61 (2007).
7. Huberman, A. D., Feller, M. B. & Chapman, B. Mechanisms underlying development of visual maps and receptive fields. *Annu. Rev. Neurosci.* **31**, 479–509 (2008).
8. Feldheim, D. A. & O'Leary, D. D. Visual map development: bidirectional signaling, bifunctional guidance molecules, and competition. *Cold Spring Harb. Perspect. Biol.* **2**, a001768 (2010).
9. Huberman, A. D., Clandinin, T. R. & Baier, H. Molecular and cellular mechanisms of lamina-specific axon targeting. *Cold Spring Harb. Perspect. Biol.* **2**, a001743 (2010).
10. Luo, L. & Flanagan, J. G. Development of continuous and discrete neural maps. *Neuron* **56**, 284–300 (2007).
11. Cang, J. & Feldheim, D. A. Developmental mechanisms of topographic map formation and alignment. *Annu. Rev. Neurosci.* **36**, 51–77 (2013).
12. Clark, D. A., Freifeld, L. & Clandinin, T. R. Mapping and cracking sensorimotor circuits in genetic model organisms. *Neuron* **78**, 583–595 (2013).
13. Murphy, K., James, L. S., Sakata, J. T. & Prather, J. F. Advantages of comparative studies in songbirds to understand the neural basis of sensorimotor integration. *J. Neurophysiol.* **118**, 800–816 (2017).
14. Buschges, A., Scholz, H. & El Manira, A. New moves in motor control. *Curr. Biol.* **21**, R513–R524 (2011).
15. Grillner, S. Biological pattern generation: the cellular and computational logic of networks in motion. *Neuron* **52**, 751–766 (2006).
16. Winding, M. et al. The connectome of an insect brain. *Science* **379**, eadd9330 (2023).
17. Eichler, K. et al. The complete connectome of a learning and memory centre in an insect brain. *Nature* **548**, 175–182 (2017).
18. Takemura, S. Y. et al. A visual motion detection circuit suggested by Drosophila connectomics. *Nature* **500**, 175–181 (2013).
19. Azevedo, A. et al. Connectomic reconstruction of a female Drosophila ventral nerve cord. *Nature* **631**, 360–368 (2024).
20. Lesser, E. et al. Synaptic architecture of leg and wing premotor control networks in Drosophila. *Nature* **631**, 369–377 (2024).
21. Dorkenwald, S. et al. Neuronal wiring diagram of an adult brain. *Nature* **634**, 124–138 (2024).
22. Garner, D. et al. Connectomic reconstruction predicts visual features used for navigation. *Nature* **634**, 181–190 (2024).
23. Lin, A. et al. Network statistics of the whole-brain connectome of Drosophila. *Nature* **634**, 153–165 (2024).
24. Matsliah, A. et al. Neuronal parts list and wiring diagram for a visual system. *Nature* **634**, 166–180 (2024).
25. Pospisil, D. A. et al. The fly connectome reveals a path to the effectome. *Nature* **634**, 201–209 (2024).
26. Sapkal, N. et al. Neural circuit mechanisms underlying context-specific halting in Drosophila. *Nature* **634**, 191–200 (2024).
27. Schlegel, P. et al. Whole-brain annotation and multi-connectome cell typing of Drosophila. *Nature* **634**, 139–152 (2024).
28. Shiu, P. K. et al. A Drosophila computational brain model reveals sensorimotor processing. *Nature* **634**, 210–219 (2024).
29. Jefferis, G. S., Marin, E. C., Stocker, R. F. & Luo, L. Target neuron prespecification in the olfactory map of Drosophila. *Nature* **414**, 204–208 (2001).

30. Jefferis, G. S. et al. Developmental origin of wiring specificity in the olfactory system of Drosophila. *Development* **131**, 117–130 (2004).
31. Marin, E. C., Watts, R. J., Tanaka, N. K., Ito, K. & Luo, L. Developmentally programmed remodeling of the Drosophila olfactory circuit. *Development* **132**, 725–737 (2005).
32. Yu, H. H. et al. A complete developmental sequence of a Drosophila neuronal lineage as revealed by twin-spot MARCM. *PLoS Biol.* **8**, e1000461 (2010).
33. Wong, K. K. L. et al. Origin of wiring specificity in an olfactory map revealed by neuron type-specific, time-lapse imaging of dendrite targeting. *Elife* **12**, e85521 (2023).
34. Komiyama, T., Johnson, W. A., Luo, L. & Jefferis, G. S. From lineage to wiring specificity. POU domain transcription factors control precise connections of Drosophila olfactory projection neurons. *Cell* **112**, 157–167 (2003).
35. Komiyama, T., Sweeney, L. B., Schuldiner, O., Garcia, K. C. & Luo, L. Graded expression of semaphorin-1a cell-autonomously directs dendritic targeting of olfactory projection neurons. *Cell* **128**, 399–410 (2007).
36. Li, H. et al. Classifying Drosophila olfactory projection neuron subtypes by single-cell RNA sequencing. *Cell* **171**, 1206–1220 e1222 (2017).
37. Xie, Q. et al. Transcription factor Acj6 controls dendrite targeting via a combinatorial cell-surface code. *Neuron* **110**, 2299–2314 e2298 (2022).
38. Sink, H. & Whitington, P. M. Location and connectivity of abdominal motoneurons in the embryo and larva of Drosophila melanogaster. *J. Neurobiol.* **22**, 298–311 (1991).
39. Bossing, T. & Technau, G. M. The fate of the CNS midline progenitors in Drosophila as revealed by a new method for single cell labelling. *Development* **120**, 1895–1906 (1994).
40. Landgraf, M., Bossing, T., Technau, G. M. & Bate, M. The origin, location, and projections of the embryonic abdominal motorneurons of Drosophila. *J. Neurosci.* **17**, 9642–9655 (1997).
41. Schmidt, H. et al. The embryonic central nervous system lineages of Drosophila melanogaster. II. Neuroblast lineages derived from the dorsal part of the neuroectoderm. *Dev. Biol.* **189**, 186–204 (1997).
42. Schmid, A., Chiba, A. & Doe, C. Q. Clonal analysis of Drosophila embryonic neuroblasts: neural cell types, axon projections and muscle targets. *Development* **126**, 4653–4689 (1999).
43. Keshishian, H., Broadie, K., Chiba, A. & Bate, M. The drosophila neuromuscular junction: a model system for studying synaptic development and function. *Annu. Rev. Neurosci.* **19**, 545–575 (1996).
44. Landgraf, M., Jeffrey, V., Fujioka, M., Jaynes, J. B. & Bate, M. Embryonic origins of a motor system: motor dendrites form a myotopic map in Drosophila. *PLoS Biol.* **1**, E41 (2003).
45. Furrer, M. P., Kim, S., Wolf, B. & Chiba, A. Robo and Frazzled/DCC mediate dendritic guidance at the CNS midline. *Nat. Neurosci.* **6**, 223–230 (2003).
46. Furrer, M. P., Vasenkova, I., Kamiyama, D., Rosado, Y. & Chiba, A. Slit and Robo control the development of dendrites in Drosophila CNS. *Development* **134**, 3795–3804 (2007).
47. Mauss, A., Tripodi, M., Evers, J. F. & Landgraf, M. Midline signalling systems direct the formation of a neural map by dendritic targeting in the Drosophila motor system. *PLoS Biol.* **7**, e1000200 (2009).
48. Ou, Y., Chwalla, B., Landgraf, M. & van Meyel, D. J. Identification of genes influencing dendrite morphogenesis in developing peripheral sensory and central motor neurons. *Neural Dev.* **3**, 16 (2008).
49. Tripodi, M., Evers, J. F., Mauss, A., Bate, M. & Landgraf, M. Structural homeostasis: compensatory adjustments of dendritic arbor geometry in response to variations of synaptic input. *PLoS Biol.* **6**, e260 (2008).
50. Landgraf, M. & Thor, S. Development of Drosophila motoneurons: specification and morphology. *Semin Cell Dev. Biol.* **17**, 3–11 (2006).
51. Kamiyama, D. & Chiba, A. Endogenous activation patterns of Cdc42 GTPase within Drosophila embryos. *Science* **324**, 1338–1340 (2009).
52. Kamiyama, D. et al. Specification of Dendritogenesis Site in Drosophila aCC Motoneuron by Membrane Enrichment of Pak1 through Dscam1. *Dev. Cell* **35**, 93–106 (2015).
53. Bui, K. C. & Kamiyama, D. Adjacent neuronal fascicle guides Motoneuron 24 dendritic branching and axonal routing decisions through Dscam1 Signaling. *eNeuro*, **11**, ENEURO.0130-24.2024 (2024).
54. Santiago, C. & Bashaw, G. J. Islet coordinately regulates motor axon guidance and dendrite targeting through the frazzled/DCC receptor. *Cell Rep.* **18**, 1646–1659 (2017).
55. Seroka, A. Q. & Doe, C. Q. The Hunchback temporal transcription factor determines motor neuron axon and dendrite targeting in Drosophila. *Development* **146**, dev175570 (2019).
56. Sanchez-Soriano, N. et al. Are dendrites in Drosophila homologous to vertebrate dendrites?. *Dev. Biol.* **288**, 126–138 (2005).
57. Kim, S. & Chiba, A. Dendritic guidance. *Trends Neurosci.* **27**, 194–202 (2004).
58. Brierley, D. J., Blanc, E., Reddy, O. V., Vijayraghavan, K. & Williams, D. W. Dendritic targeting in the leg neuropil of Drosophila: the role of midline signalling molecules in generating a myotopic map. *PLoS Biol.* **7**, e1000199 (2009).
59. Bement, W. M., Goryachev, A. B., Miller, A. L. & von Dassow, G. Patterning of the cell cortex by Rho GTPases. *Nat. Rev. Mol. Cell Biol.* **25**, 290–308 (2024).
60. Hall, A. Rho GTPases and the actin cytoskeleton. *Science* **279**, 509–514 (1998).
61. Nalbant, P., Hodgson, L., Kraynov, V., Toutchkine, A. & Hahn, K. M. Activation of endogenous Cdc42 visualized in living cells. *Science* **305**, 1615–1619 (2004).
62. Itoh, R. E. et al. Activation of Rac and cdc42 video imaged by fluorescent resonance energy transfer-based single-molecule probes in the membrane of living cells. *Mol. Cell Biol.* **22**, 6582–6591 (2002).
63. Wakayama, Y., Fukuhara, S., Ando, K., Matsuda, M. & Mochizuki, N. Cdc42 mediates Bmp-induced sprouting angiogenesis through Fmnl3-driven assembly of endothelial filopodia in zebrafish. *Dev. Cell* **32**, 109–122 (2015).
64. Kamemura, K. & Chihara, T. Multiple functions of the ER-resident VAP and its extracellular role in neural development and disease. *J. Biochem* **165**, 391–400 (2019).
65. Petkovic, M., O'Brien, C. E. & Jan, Y. N. Interorganelle communication, aging, and neurodegeneration. *Genes Dev.* **35**, 449–469 (2021).
66. Landers, J. E. et al. New VAPB deletion variant and exclusion of VAPB mutations in familial ALS. *Neurology* **70**, 1179–1185 (2008).
67. Fasana, E. et al. A VAPB mutant linked to amyotrophic lateral sclerosis generates a novel form of organized smooth endoplasmic reticulum. *FASEB J.* **24**, 1419–1430 (2010).
68. Kabashi, E. et al. Investigating the contribution of VAPB/ALS8 loss of function in amyotrophic lateral sclerosis. *Hum. Mol. Genet.* **22**, 2350–2360 (2013).
69. Inal, M. A., Banzai, K. & Kamiyama, D. Retrograde Tracing of Drosophila Embryonic Motor Neurons Using Lipophilic Fluorescent Dyes. *J. Vis. Exp.* **155**, e60716 (2020).
70. Fujioka, M. et al. Even-skipped, acting as a repressor, regulates axonal projections in Drosophila. *Development* **130**, 5385–5400 (2003).

71. Malartre, M., Ayaz, D., Amador, F. F. & Martin-Bermudo, M. D. The guanine exchange factor vav controls axon growth and guidance during Drosophila development. *J. Neurosci.* **30**, 2257–2267 (2010).
72. Rodriguez-Fdez, S. & Bustelo, X. R. The Vav GEF family: an evolutionary and functional perspective. *Cells* **8**, 465 (2019).
73. Sinha, S. & Yang, W. Cellular signaling for activation of Rho GTPase Cdc42. *Cell Signal* **20**, 1927–1934 (2008).
74. Harris, K. P. & Tepass, U. Cdc42 and vesicle trafficking in polarized cells. *Traffic* **11**, 1272–1279 (2010).
75. Chen, C., Wirth, A. & Ponimaskin, E. Cdc42: an important regulator of neuronal morphology. *Int J. Biochem. Cell Biol.* **44**, 447–451 (2012).
76. Boyle, M., Nighorn, A. & Thomas, J. B. Drosophila Eph receptor guides specific axon branches of mushroom body neurons. *Development* **133**, 1845–1854 (2006).
77. Cowan, C. W. et al. Vav family GEFs link activated Ephs to endocytosis and axon guidance. *Neuron* **46**, 205–217 (2005).
78. Binns, K. L., Taylor, P. P., Sicheri, F., Pawson, T. & Holland, S. J. Phosphorylation of tyrosine residues in the kinase domain and juxtamembrane region regulates the biological and catalytic activities of Eph receptors. *Mol. Cell Biol.* **20**, 4791–4805 (2000).
79. Fang, W. B., Brantley-Sieders, D. M., Hwang, Y., Ham, A. J. & Chen, J. Identification and functional analysis of phosphorylated tyrosine residues within EphA2 receptor tyrosine kinase. *J. Biol. Chem.* **283**, 16017–16026 (2008).
80. Martin-Bermudo, M. D., Bardet, P. L., Bellaiche, Y. & Malartre, M. The vav oncogene antagonises EGFR signalling and regulates adherens junction dynamics during Drosophila eye development. *Development* **142**, 1492–1501 (2015).
81. Tsuda, H. et al. The amyotrophic lateral sclerosis 8 protein VAPB is cleaved, secreted, and acts as a ligand for Eph receptors. *Cell* **133**, 963–977 (2008).
82. Anzo, M. et al. Dendritic Eph organizes dendrodendritic segregation in discrete olfactory map formation in Drosophila. *Genes Dev.* **31**, 1054–1065 (2017).
83. Seroka, A., Lai, S. L. & Doe, C. Q. Transcriptional profiling from whole embryos to single neuroblast lineages in Drosophila. *Dev. Biol.* **489**, 21–33 (2022).
84. Brunet Avalos, C., Maier, G. L., Bruggmann, R. & Sprecher, S. G. Single cell transcriptome atlas of the Drosophila larval brain. *Elife* **8**, e50354 (2019).
85. Zlatic, M., Li, F., Strigini, M., Grueber, W. & Bate, M. Positional cues in the Drosophila nerve cord: semaphorins pattern the dorso-ventral axis. *PLoS Biol.* **7**, e1000135 (2009).
86. Kim, M. D., Wen, Y. & Jan, Y. N. Patterning and organization of motor neuron dendrites in the Drosophila larva. *Dev. Biol.* **336**, 213–221 (2009).
87. Petty, A. et al. A small molecule agonist of EphA2 receptor tyrosine kinase inhibits tumor cell migration in vitro and prostate cancer metastasis in vivo. *PLoS One* **7**, e42120 (2012).
88. Petty, A. et al. Design and synthesis of small molecule agonists of EphA2 receptor. *Eur. J. Med Chem.* **143**, 1261–1276 (2018).
89. Luo, L., Liao, Y. J., Jan, L. Y. & Jan, Y. N. Distinct morphogenetic functions of similar small GTPases: Drosophila Drac1 is involved in axonal outgrowth and myoblast fusion. *Genes Dev.* **8**, 1787–1802 (1994).
90. Harden, N., Loh, H. Y., Chia, W. & Lim, L. A dominant inhibitory version of the small GTP-binding protein Rac disrupts cytoskeletal structures and inhibits developmental cell shape changes in Drosophila. *Development* **121**, 903–914 (1995).
91. Hariharan, I. K. et al. Characterization of rho GTPase family homologues in Drosophila melanogaster: overexpressing Rho1 in retinal cells causes a late developmental defect. *EMBO J.* **14**, 292–302 (1995).
92. Kim, M. D., Kamiyama, D., Kolodziej, P., Hing, H. & Chiba, A. Isolation of Rho GTPase effector pathways during axon development. *Dev. Biol.* **262**, 282–293 (2003).
93. Genova, J. L., Jong, S., Camp, J. T. & Fehon, R. G. Functional analysis of Cdc42 in actin filament assembly, epithelial morphogenesis, and cell signaling during Drosophila development. *Dev. Biol.* **221**, 181–194 (2000).
94. Dearborn, R. E. Jr et al. Reph, a regulator of Eph receptor expression in the Drosophila melanogaster optic lobe. *PLoS One* **7**, e37303 (2012).
95. Buhl, E. et al. Effects of Eph/ephrin signalling and human Alzheimer's disease-associated EphA1 on Drosophila behaviour and neurophysiology. *Neurobiol. Dis.* **170**, 105752 (2022).
96. Lev, S., Ben Halevy, D., Peretti, D. & Dahan, N. The VAP protein family: from cellular functions to motor neuron disease. *Trends Cell Biol.* **18**, 282–290 (2008).
97. Weir, M. L., Klip, A. & Trimble, W. S. Identification of a human homologue of the vesicle-associated membrane protein (VAMP)-associated protein of 33 kDa (VAP-33): a broadly expressed protein that binds to VAMP. *Biochem J.* **333**, 247–251 (1998).
98. Nishimura, Y., Hayashi, M., Inada, H. & Tanaka, T. Molecular cloning and characterization of mammalian homologues of vesicle-associated membrane protein-associated (VAMP-associated) proteins. *Biochem. Biophys. Res Commun.* **254**, 21–26 (1999).
99. Peretti, D., Dahan, N., Shimoni, E., Hirschberg, K. & Lev, S. Coordinated lipid transfer between the endoplasmic reticulum and the Golgi complex requires the VAP proteins and is essential for Golgi-mediated transport. *Mol. Biol. Cell* **19**, 3871–3884 (2008).
100. Mikitova, V. & Levine, T. P. Analysis of the key elements of FFAT-like motifs identifies new proteins that potentially bind VAP on the ER, including two AKAPs and FAPP2. *PLoS One* **7**, e30455 (2012).
101. Kuijpers, M. et al. The ALS8 protein VAPB interacts with the ER-Golgi recycling protein YIF1A and regulates membrane delivery into dendrites. *EMBO J.* **32**, 2056–2072 (2013).
102. Han, S. M. et al. Secreted VAPB/ALS8 major sperm protein domains modulate mitochondrial localization and morphology via growth cone guidance receptors. *Dev. Cell* **22**, 348–362 (2012).
103. Kamemura, K. et al. Secretion of endoplasmic reticulum protein VAPB/ALS8 requires topological inversion. *Nat. Commun.* **15**, 8777 (2024).
104. O'Connor, D. M. & Boulis, N. M. Cellular and molecular approaches to motor neuron therapy in amyotrophic lateral sclerosis and spinal muscular atrophy. *Neurosci. Lett.* **527**, 78–84 (2012).
105. Bowerman, M. et al. Pathogenic commonalities between spinal muscular atrophy and amyotrophic lateral sclerosis: Converging roads to therapeutic development. *Eur. J. Med. Genet* **61**, 685–698 (2018).
106. Nishimura, A. L. et al. A mutation in the vesicle-trafficking protein VAPB causes late-onset spinal muscular atrophy and amyotrophic lateral sclerosis. *Am. J. Hum. Genet.* **75**, 822–831 (2004).
107. Funke, A. D. et al. The p.P56S mutation in the VAPB gene is not due to a single founder: the first European case. *Clin. Genet.* **77**, 302–303 (2010).
108. Chen, H. J. et al. Characterization of the properties of a novel mutation in VAPB in familial amyotrophic lateral sclerosis. *J. Biol. Chem.* **285**, 40266–40281 (2010).
109. van Blitterswijk, M. et al. VAPB and C9orf72 mutations in 1 familial amyotrophic lateral sclerosis patient. *Neurobiol. Aging* **33**, 2950 e2951–2950 e2954 (2012).
110. Teuling, E. et al. Motor neuron disease-associated mutant vesicle-associated membrane protein-associated protein (VAP) B recruits wild-type VAPs into endoplasmic reticulum-derived tubular aggregates. *J. Neurosci.* **27**, 9801–9815 (2007).
111. Suzuki, H. et al. ALS-linked P56S-VAPB, an aggregated loss-of-function mutant of VAPB, predisposes motor neurons to ER stress-

related death by inducing aggregation of co-expressed wild-type VAPB. *J. Neurochem.* **108**, 973–985 (2009).

112. Prosser, D. C., Tran, D., Gougeon, P. Y., Verly, C. & Ngsee, J. K. FFAT rescues VAPA-mediated inhibition of ER-to-Golgi transport and VAPB-mediated ER aggregation. *J. Cell Sci.* **121**, 3052–3061 (2008).
113. Genevini, P. et al. Amyotrophic lateral sclerosis-linked mutant VAPB inclusions do not interfere with protein degradation pathways or intracellular transport in a cultured cell model. *PLoS One* **9**, e113416 (2014).
114. Gkogkas, C., Wardrope, C., Hannah, M. & Skehel, P. The ALS8-associated mutant VAPB(P56S) is resistant to proteolysis in neurons. *J. Neurochem* **117**, 286–294 (2011).
115. Borgese, N., Iacomino, N., Colombo, S. F. & Navone, F. The link between VAPB loss of function and amyotrophic lateral sclerosis. *Cells* **10**, 1865 (2021).
116. Deidda, I. et al. Expression of vesicle-associated membrane-protein-associated protein B cleavage products in peripheral blood leukocytes and cerebrospinal fluid of patients with sporadic amyotrophic lateral sclerosis. *Eur. J. Neurol.* **21**, 478–485 (2014).
117. McHanwell, S. & Biscoe, T. J. The localization of motoneurons supplying the hindlimb muscles of the mouse. *Philos. Trans. R. Soc. Lond. B Biol. Sci.* **293**, 477–508 (1981).
118. Vanderhorst, V. G. & Holstege, G. Organization of lumbosacral motoneuronal cell groups innervating hindlimb, pelvic floor, and axial muscles in the cat. *J. Comp. Neurol.* **382**, 46–76 (1997).
119. Vrieseling, E. & Arber, S. Target-induced transcriptional control of dendritic patterning and connectivity in motor neurons by the ETS gene Pea3. *Cell* **127**, 1439–1452 (2006).
120. Katsuki, T., Ailani, D., Hiramoto, M. & Hiromi, Y. Intra-axonal patterning: intrinsic compartmentalization of the axonal membrane in Drosophila neurons. *Neuron* **64**, 188–199 (2009).

Acknowledgements

We thank Edward Kipreos, Kota Banzai, Kousuke Kamemura, and the members of the Kamiyama lab for their valuable feedback on our manuscript. We are thankful for the generous provision of reagents from Thomas Kidd, Marianne Malartre, Hiroshi Tsuda, and Hugo Bellen. We also acknowledge the use of stocks from the Bloomington Drosophila Stock Center (NIH P40OD18537). This research was supported by NIH R01 NS107558 (to Y.N., R.K., A.S., G.B.V., K.C.B., M.F. and D.K.), start-up funds from the University of Georgia (to H.D., and O.A), JSPS KAKENHI (Grant Number 21H02479), and the Astellas Foundation for Research on Metabolic Disorders (to T.C.).

Author contributions

T.C. and D.K. conceptualized and designed the project. The experiments were conducted by D.K., R.K., Y.N., G.B.V. and K.C.B. Reagents were produced by R.K. and M.F. Data analysis was carried out by D.K., R.K., A.S., H.D. and O.A. The manuscript was primarily written by D.K. and subsequently edited by R.K., Y.N., A.S., G.B.V., K.C.B., M.F., H.D., O.A., and T.C.

Competing interests

The authors declare no competing interests.

Additional information

Supplementary information The online version contains supplementary material available at https://doi.org/10.1038/s41467-025-65900-y.

Correspondence and requests for materials should be addressed to Daichi Kamiyama.

Peer review information *Nature Communications* thanks the anonymous reviewer(s) for their contribution to the peer review of this work. A peer review file is available.

Reprints and permissions information is available at http://www.nature.com/reprints